Università degli Studi di Milano

Facoltà di Scienze e Tecnologie

Corso di Laurea Magistrale in Fisica

Electron Beam Measurements with Beam Loss Monitors in AWAKE

Relatore:
Prof. Massimo SORBI
Relatore Esterno:
Dr. Marlene TURNER

Tesi di Laurea di:
Livio VERRA
Matricola:
897045

Anno Accademico 2017/2018

Affidavit

I declare that I have authored this thesis independently, that I have not used other than the declared sources/resources, and that I have explicitly indicated all material which has been quoted either literally or by content from the sources used. The text document uploaded to UNIMI is identical to the present Master's Thesis.

A chi mi ha permesso di essere qui,
a chi mi ha indicato la via,
a chi l'ha percorsa con me,
a chi c'è stato, fino alla fine.

”Da te stesso non ci scappi
nemmeno se sei Eddie Merckx.”

Abstract

In this thesis I study experimentally electron beam loss signals in AWAKE, the Advanced WAKEfield experiment at CERN. In AWAKE, electrons are accelerated by obliquely injecting them into the plasma wakefields driven by a self-modulating relativistic proton bunch.

Due to the complexity of the 10 meter long vapor source that provides the plasma, we have to transport and inject the electrons through a 10 mm diameter entrance aperture. I designed, simulated and implemented a diagnostic system to study physics properties of the external injection of the 18 MeV/c electron bunch into the plasma.

We have installed seven scintillating detectors along the plasma as electron beam loss monitors. Each detector measures the secondary particles produced when the electron bunch interacts with material.

To prove the feasibility of the system and to support understanding of the results, I run FLUKA simulations of the setup. According to simulations, secondary particles can exit the vapor source and their energy deposition in the detectors is above the detection threshold of 100 keV. The spatial resolution, determined by the distance between individual detectors, allows to estimate where the beam is lost and whether it interacts with the material surrounding the entrance aperture.

We measured the electron transverse beam size at the aperture location, for different beam focus positions and beam charges, scanning the electron beam across the vapor source entrance aperture, while recording the beam loss monitor signals. For the 200 pC electron bunch, the r.m.s. transverse beam size (σ_x, σ_y) at the entrance increases from $(0.45 \pm 0.02,\ 0.33 \pm 0.04)$ mm to $(2.6 \pm 0.4,\ 0.9 \pm 0.1)$ mm as the beam is focused further inside the plasma. Furthermore, I observed the beam size to increase with the charge as $\sigma_{600} \sim \sqrt{2}\sigma_{200}$ (where σ_{600} and σ_{200} are the r.m.s. beam sizes for the 600 and 200 pC beams

respectively), as expected from theoretical predictions.

Spatial electron, proton and laser beam alignment is one of the crucial issues of the AWAKE experiment; therefore, we were interested in quantifying the deviation caused by the earth magnetic field on the electron beam trajectory in order to precisely overlap the beams. Aligning the electron beam onto a proton reference trajectory and scanning both beams across the aperture, I estimated the deflection from the straight trajectory to be: (1.2 ± 0.1) mm in the horizontal plane (bending to the right) and (0.4 ± 0.1) mm in the vertical plane (bending downward).

Beam loss detection gives also information on the beam propagation along the vapor source. I estimated electron beam losses at the entrance for different beam focusing optics and studied the propagation of electrons in vacuum and within the plasma channel.

During the acceleration experiment, at the presence of proton driven wakefields, I observed an increase of electron losses downstream the injection point. This may be explained considering defocusing wakefields acting on part of the injected electron bunch.

Additionally, studying the background generated by the proton beam on the beam loss monitors, I observed satellite pre-bunches ahead of the main proton bunch delivered by the CERN Super Proton Synchrotron.

Contents

Chapter 1

Introduction

1.1 Why is plasma wakefield acceleration interesting?

Particle physicists explore the smallest building blocks of nature and the forces between them by colliding high-energy particles using accelerators. Higher collision energies allow the creation of higher mass particles and also correspond to resolving smaller structures.

Conventional accelerators accelerate charged particles using the longitudinal electric field created by radio-frequency (RF) cavities. The maximum field of RF cavities is intrinsically limited by the electric breakdown of the structure to $\sim 100\,\mathrm{MV/m}$. This means that an electron can gain for example 1 GeV in 10 m.

Plasmas can sustain higher electric fields strengths, because they consist of ionized particles. The strength of the electric fields created by plasma oscillations depends on the amount of electron charge that is displaced and on the charge separation distance. The maximum fields that can be created at a given plasma density n_{pe} can be estimated by the cold-plasma non-relativistic wavebreaking field E_{max}:

$$E_{\mathrm{max}} \approx \frac{m_{\mathrm{e}} \cdot c \cdot \omega_{\mathrm{pe}}}{e} \sim 100 \frac{V}{m} \sqrt{n_{\mathrm{pe}}[cm^{-3}]} \qquad (1.1)$$

where m_e is the electron mass at rest, c is the speed of light, ω_{pe} is the plasma electron angular frequency and e the electron charge.

For example, the maximum field E_{max} reaches 1 GV/m for a plasma electron density of 10^{14} cm^{-3} or 100 GV/m for a plasma electron density of 10^{18} cm^{-3}.

In 1979, T. Tajima and J.M. Dawson proposed that laser driven plasma oscillations can trap and accelerate electrons [1]. The experimental realization followed in 1992 by C. Clayton using a laser plasma beatwave accelerator [2]. Laser plasma wakefield experiments became possible with the invention of chirped pulse amplification (CPA) [3].

In 1985 P. Chen et al. suggested that the plasma waves can also be driven by a relativistic electron beam [4]. The demonstration followed by J. Rosenzweig in 1988 [5]. Experiments at SLAC in 2007 demonstrated that electrons were accelerated from 42 to 84 GeV in 85 cm of plasma (average accelerating gradient $\sim 50\,\mathrm{GV/m}$) [6].

1.1.1 The importance of high accelerating gradient

Protons versus electrons or positrons accelerators

Protons are composite particles consisting of quarks and gluons and the proton mass m_p is $1.6 \cdot 10^{-27}$ kg or $936\,\mathrm{MeV/c^2}$. Electrons (and positrons) are elementary, point-like particles with a mass of $m_e = 9.1 \cdot 10^{-31}$ kg or $0.511\,\mathrm{MeV/c^2}$. We note that the proton mass is 1836 times heavier than the electron mass.

Proton colliders are often called "discovery machines" because in proton-proton collisions quarks and gluons collide with high energies, although individually undefined. On the other hand electron-positron or electron-electron colliders are "precision machines" because two point like particles collide with well-defined energy.

Circular versus linear acceleration

Currently, there are two main geometries to accelerate particles to very high energies: linear and circular accelerators. Circular particle accelerators (for example CERN's Large Hadron Collider (LHC)) bend charged particles on a circular trajectory using the field of magnetic dipoles. Particles gain energy every turn as they pass through an accelerating section, but they loose energy due to synchrotron radiation. The amount of energy loss of a relativistic particle by synchrotron radiation over one turn U_0 is [7]:

$$U_0 = \frac{e^2}{3\epsilon_0}\frac{\beta^3\gamma^4}{\rho_\mathrm{b}} \propto \frac{1}{\rho_\mathrm{b}}\frac{{E_\mathrm{p}}^4}{{m_0}^4}, \tag{1.2}$$

where ϵ_0 is the vacuum permittivity, $\beta= v_b/c$ with v_b the particle velocity, γ is the Lorentz factor, $\rho_\text{b} = \gamma m_0 c/qB_0$ is the bending radius of the charged particles in the magnetic field B_0, E_p is the particle energy and m_0 is the particle mass at rest. Equation 1.2 shows that the energy loss per turn depends on the particle energy and mass at rest to the power four and only linearly with the bending radius ρ_b. This makes circular accelerators unfavourable for the acceleration of light particles such as electrons and positrons, but favoureable for heavier particles like protons and ions.

Due to the limited energy gain per turn (equivalent for protons and electrons) and the synchrotron radiation loss, the energy that electrons and positrons reach in circular colliders is significantly lower than the energy that protons reach. For example, in the LHC, protons are accelerated to 7 TeV in a ring with a circumference of 26.659 km and the corresponding average bending radius is 4.24 km. To compare, in the same nowadays LHC tunnel the Large Electron Positron collider upgrade (LEP2) was accelerating electrons and positrons to a maximum energy of 104.5 GeV, limited by synchrotron radiation loss (at this maximum energy, $U_0 \sim 2.8$ GeV $\approx$ the gain per turn). Linear particle accelerators (e.g. the Stanford Linear Collider) consist of many and long accelerating sections. Since no dipole bending is needed, the synchrotron radiation loss is negligible. The energy the particles acquire is the product of the accelerator length and accelerating gradient, since the particles pass only once. There are two ways to reach higher particle energies in a linear particle accelerator: a longer accelerator or a larger accelerating gradient. Stronger accelerating gradients decrease the size of the accelerating sections in such a linear machine.

A high gradient acceleration technique is therefore desired. Plasma wakefield acceleration holds the potential of high accelerating gradients.

1.1.2 Future linear collider proposals

One current proposal for a conventional (using RF technology) linear electron-positron collider is the Compact Linear Collider project, also called CLIC [8]. CLIC aims to accelerate electrons and positrons to 1.5 TeV per beam using accelerating structures with an electric field of 100 MV/m. The length of the machine would be about 42 km, and the estimated cost about (27 ± 8) Billion US Dollar [9].

Adli et al. proposed a linear plasma-wakefield collider driven by electron bunches. In this design, the collider is 4.5 km long, and accelerates electrons and positrons up to 0.5 TeV each. The wakefields are driven in stages, by 25 GeV electron bunches, and the average acceleration gradient is 7.6 GV/m [10]. Leeman et al. proposed a linear 2 TeV electron–positron collider based on laser-driven plasma acceleration with a length of ~ 1 km and about 100 1 m-long stages. For each stage, a 30 J laser pulse drives plasma wakefields and creates accelerating gradients of 10 GeV/m [11].

The possibility of accelerating electrons up to 600 GeV in 600 m of plasma, where the wakefields are driven by a LHC type 7 TeV proton drive bunch, was suggested in 2009 by Allen Caldwell et al. [12]. In this design high energy electrons would collide with high energy protons.

At this moment, the RF acceleration technique is much more advanced than plasma wakefield acceleration. But a future linear collider based on plasma wakefield acceleration could be considerably more compact than one using conventional RF technology.

1.2 The AWAKE experiment at CERN

AWAKE [13], the Advanced WAKEfield project is a proof-of-principle R&D experiment at CERN. The first goal of AWAKE was to demonstrate and study seeded proton bunch self-modulation [14] and resonant excitation of strong plasma wakefields. The second goal was to use the wakefields to accelerate an externally injected electron witness bunch. In the longer term, the goal is to accelerate electrons to $10 - 100$ GeV, or possibly TeV, for electron fixed-target and electron/positron experiments [15].

The commissioning of the experimental area, the proton and the laser beamline was performed in autumn of 2016. After the commissioning period, the experiment was ready for AWAKE Run 1-Phase 1 (2016-2017). Run 1-Phase 1 was dedicated to the measurement and understanding of the seeded self-modulation (SSM) of a long proton bunch in plasma. Simultaneously ongoing was the installation and later commissioning of the electron beamline (2017). After the completion of the electron beamline AWAKE was ready for Run 1-Phase 2 in which the experiment successfully accelerated externally injected electrons in the created plasma wakefield (2018) [16]. Figure 1.1 shows accelerated electrons imaged on the scintillating spectrometer screen.

The AWAKE collaboration is currently preparing for AWAKE Run 2, which is planned to take place after the two-year long shut-down of the CERN accel-

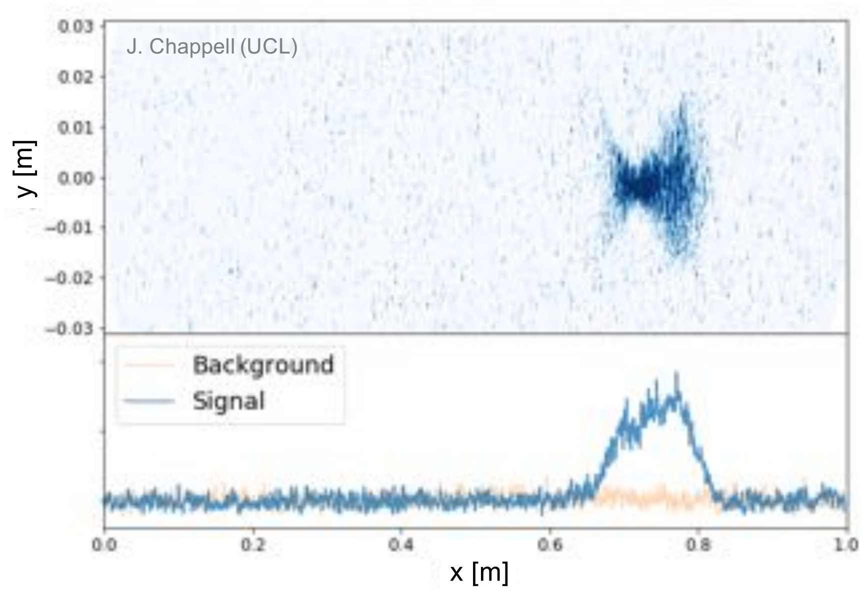

Figure 1.1: Accelerated electrons observed on the electron spectrometer scintillating screen. The beam energy is dispersed by a dipole magnetic field and thus energy resolved. The plot underneath shows the projection lines when beam is present (blue line) and for the background (orange).

erator complex. The goal of Run 2 is to improve the technique developed in the first Run and to create a tens of GeV electron bunch with low emittance ($\sim 1\,$mm·mrad) and low relative energy spread ($\sim 1\,\%$).

1.2.1 Motivation for using a proton driven bunch

The distance over which plasma wakefields can be driven depends on the energy stored in the drive bunch. In AWAKE, protons drive the plasma waves. The total energy E stored in one particle is:

$$E = \gamma m_0 c^2, \tag{1.3}$$

where γ is the Lorentz factor given by:

$$\gamma = \sqrt{1 + (\frac{p}{m_0 c})^2}, \tag{1.4}$$

p is the particle momentum and m_0 is the particle rest mass.

Thus, a 400 GeV/c proton drive bunch provided by the CERN Super Proton Synchrotron (SPS) with $3{\cdot}10^{11}$ particles sent to AWAKE contains $\sim$ 20 kJ. To compare, the 42 GeV electon bunch with $1.8{\cdot}10^{10}$ particles at SLAC only carries and energy of 0.12 kJ. The higher the energy stored in the drive bunch, the longer distance it can excite wakefields along the plasma. Using the SPS proton bunch, AWAKE can accelerate electrons to high energy in a single stage.

1.2.2 General layout

A schematic layout of the AWAKE experiment is shown in Figure 1.2.

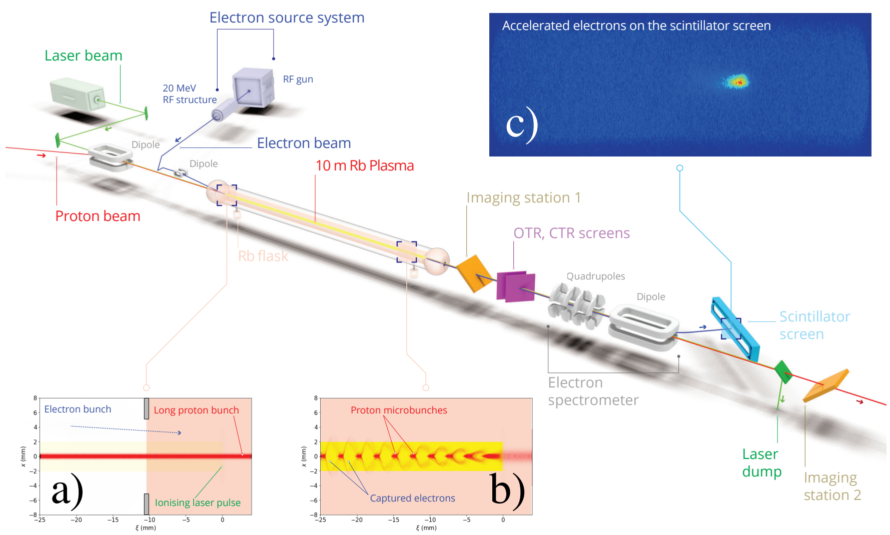

Figure 1.2: Schematic layout of the AWAKE facility. Proton (red), laser (green) and electron (blue) beams are merged upstream the Rb source (yellow cylinder). Proton beam diagnostics (Imaging Stations, OTR and CTR screens) and the electron spectrometer are positioned downstream the plasma. (a) is a schematic of the beam injection geometry at the entrance; (b) shows the modulated proton bunch and captured electrons at the exit of the plasma. (c) is an image of the accelerated electron beam on the scintillating spectrometer screen.

The core of the experiment is a 10 m long rubidium vapor source (see Figure 1.3): a long fluid-heated heat-exchanger evaporates Rb at $180-230$ °C to reach the required Rb vapor density of $0.5-10\cdot10^{14}$ atoms/cm^3. The rubidium vapor is then ionized by a 100 fs, < 450 mJ laser pulse ($\lambda = 780$ nm) creating a plasma channel with a radius of approximately 1 mm [17].

Figure 1.3: Photograph of the rubidium vapor source installed in AWAKE.

Upstream the plasma three beamlines merge, bringing together:

- the proton bunch from the CERN SPS (red in Figure 1.2), to drive plasma wakefields;
- the laser pulse (green) to ionize the rubidium vapor and seed the SSM;
- the witness electron bunch (green) to be accelerated.

The baseline temporal overlap of the three bunches is shown in Figure 1.4: the laser pulse (red) is in the middle of the proton bunch (orange) to seed the SSM and the electron bunch (blue) is located at $\sim 1\,\sigma$ of the proton bunch behind the laser pulse.

To measure the position and the transverse bunch profile of the beams (protons and electrons) along the beam-line, we use beam-position monitors (BPMs) and cameras imaging screens that emit visible light (BTVs) [18].

To observe and control the self-modulation of the proton bunch, AWAKE has two different diagnostics downstream the plasma exit: a two-screen system

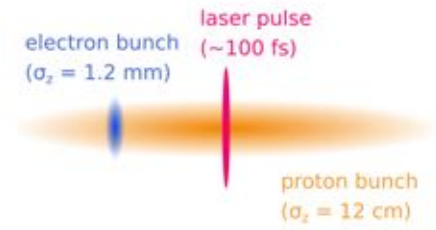

Figure 1.4: Schematic drawing of the temporal overlap of the proton, electron and laser beams.

(Imaging Stations) [19] to study the transverse profile of the proton bunch, and a streak camera that images visible light emitted by OTR (Optical Transition Radiation) [20] and CTR (Coherent Transition Radiation) [14] screens to time-resolve the longitudinal density modulation of the proton bunch at the ps-time scale.

To observe accelerated electrons, a magnetic imaging electron spectrometer is positioned downstream the plasma exit. It consists of: two quadrupoles and one dipole and one scintillating screen. The light emitted by the scintillating screen is imaged by a digital camera [21].

To study and control the injection of the electrons in the plasma, we use: BPMs, BTVs and the electron beam loss monitor (BLM) system. From these measurements we compute and predict the electron beam trajectory. The BLM setup is the topic of this thesis and will be extensively discussed later.

1.2.3 Experimental parameters

The baseline AWAKE plasma, laser pulse, proton and electron beams parameters for the injection and acceleration studies are summarized in Table 1.1.

1.2.4 The challenge of the external injection

Electrons are injected in the plasma obliquely with respect to the proton trajectory (see Figure 1.2*a*). The electron beam trajectory crosses with the plasma only once the SSM completely developed, to avoid electron defocusing at the plasma entrance.

Injection and acceleration of a low energy electron bunch ($\sim$ 18 MeV) in plasma wakefields is sensitive to plasma electron density n_{pe} variations

Parameter	**Value**
Plasma:	
Plasma type	Laser-ionized rubidum vapor
Plasma length	10 m
Plasma density	$\mathrm{n} = 0.5 - 7 \cdot 10^{14}$ electrons/cm^3
Plasma radius	$r \geq 1$ mm
Wavebreaking field $\mathrm{E_{max}} = m_e c \omega_{pe}/e$	$0.68 - 2.54$ GV/m
Laser pulse:	
Laser type	Fibre, Titanium:Sapphire
Wavelength	780 nm
Pulse length	100 fs
Laser pulse energy	< 450 mJ
Focused size at the plasma entrance	$\sigma_\mathrm{r} = 1$ mm
Proton beam:	
Bunch momentum	400 GeV/c
Protons per bunch	$3 \cdot 10^{11}$
Bunch length	$\sigma_\mathrm{z} = 12$ cm
Bunch transverse size at the plasma entrance	$\sigma_\mathrm{r} \sim 200\,\mu$m
Normalized emittance	$2 - 3$ mm·mrad
Electron beam:	
Bunch momentum	18 MeV/c
Bunch charge	$0.1 - 1$ nC
Bunch length	$\sigma_\mathrm{z} \sim 1.2$ mm
Bunch size at focus	$\sigma_\mathrm{r} > 250\,\mu$m
Normalized emittance	> 2 mm·mrad
Relative energy spread	$\Delta\mathrm{p}/\mathrm{p} = 0.5\,\%$

Table 1.1: AWAKE experimental parameters.

[22]. If n_{pe} changes, the plasma electron wavelength λ_pe changes according to $\lambda_\mathrm{pe} = 2\pi c\sqrt{m_\mathrm{e}\epsilon_0/n_\mathrm{pe}e^2}$, where: c is the speed of light, ϵ_0 is the vacuum permittivity, m_e is the rest mass of the electron, and e is the electron charge. Hence, beam electrons may dephase into the defocusing or decelerating phase of the wakefields, and exit the plasma and the wakefields.

Ideally, there would be a step transition from vacuum to plasma (with the desired n_{pe}), which could be achieved separating them with a window. Unfor-

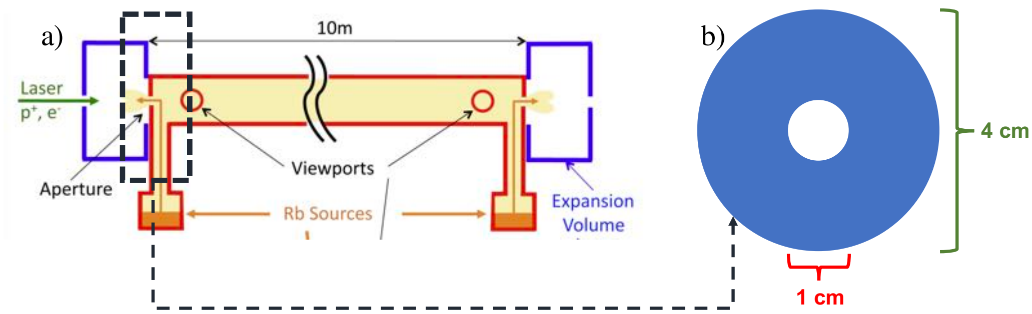

Figure 1.5: Schematic of the Rb vapor source. In (a) the transverse view: expansion volumes in blue color; in (b) the front view: aluminum foil in blue, entrance aperture in white.

tunately, there is no window through which a laser pulse, protons and electrons can propagate simultaneously. Thus, the vapor source is open at both ends with an aperture that must be large enough to allow for electron injection in different configurations (collinear and oblique).

Due to the geometry of our plasma [23], there is a short plasma electron density ramp at the plasma entrance. Each end of the vapor source is equipped with an expansion volume. Letting the Rb vapor expand in a vacuum volume with its walls maintained below the Rb condensation temperature (39.48°C) leads to a density ramp scale length on the order of the diameter of the aperture through which the vapor expands (vapor source schematics in Figure 1.5) [14]. The vapor source's entrance and exit apertures are made of 600 μm thick aluminum foils. They have a 1 cm diameter opening aperture at their center (see the front view of the plasma source in Figure 1.5b), providing a short enough density ramp (according to numerical simulation, it needs to be shorter than 10 cm [24]). The maximum injection angle is given by $\theta_{\mathrm{max}} = \min(\Delta\mathrm{y}/(\mathrm{L}+\mathrm{x}), \mathrm{r}/\mathrm{L})$, where $\Delta\mathrm{y} \sim 15$ mm is the maximum vertical offset (given by the maximum current the last corrector magnets can sustain), L is the distance between the electron-wakefield crossing point and the plasma entrance (in meters), $\mathrm{x} = 3.4$ m is the distance between the last corrector magnet and the plasma entrance, and $r = 5$ mm is the entrance aperture radius [25].

1.3 Topic of this thesis

During Run 1-Phase 2 (2018), AWAKE aimed to experimentally demonstrate the acceleration of an externally injected electron beam with proton driven plasma wakefields. The AWAKE electron beam loss monitor system is a diagnostics used for these measurements. Using the BLMs, we measure important electron beam parameters at the plasma entrance, and monitor losses during the injection experiments. In this thesis, I discuss:

- the design and realization of the electron beam loss monitor setup;
- FLUKA simulations to prove the feasibility of the system and to support understanding of the results;
- the measurement results, including:
  - measurement of the electron transverse beam size at the entrance of the vapor source;
  - estimation of the effect of the earth magnetic field on the electron beam trajectory;
  - studies on the beam propagation along the vapor source;
  - detection of defocused electrons during the acceleration experiment.

1.3.1 The electron beam loss monitor system

The electron beam loss monitor system detects the secondary particles that are produced when particles interact with the material of the vapor source. The concept is illustrated in Figure 1.6.

Since no diagnostics can be positioned inside the plasma (there are no screens between 0.8 m upstream of the entrance and 2 m downstream of the exit of the vapor source), the loss monitors are the only system providing information on the beam along the plasma.

Using this setup, I measure the transverse size of the electron beam at the plasma entrance. I also quantify losses at this location for different electron beam focusing optics and injection alignments. In addition, I quantify the effect of the earth magnetic field on the electron beam trajectory, and I estimate the propagation of the beam along the source for different focal point position and in presence of plasma.

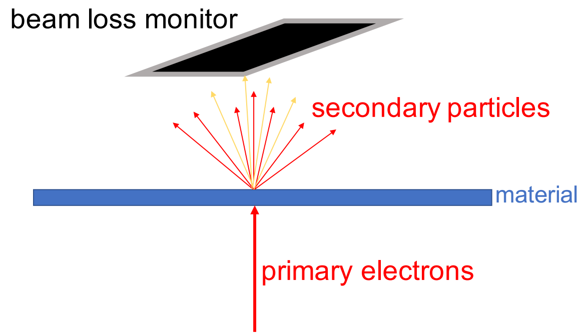

Figure 1.6: Schematic drawing of the loss production and detection. Primary electrons interact with material (e.g. vapor source layers) and produce showers of scattered electrons and photons. These secondary particles may then be detected by the BLM.

During the injection experiment, no screen can be inserted into the upstream beam path: it would either be damaged by the laser pulse or spoil emittance of the electron beam (see Figure 1.7). Thus, the only information on the electron beam is given by BPMs upstream the plasma, and by the electron spectrometer at the end of the line. With the BLM setup, I observe losses during the acceleration process and estimate their position along the plasma.

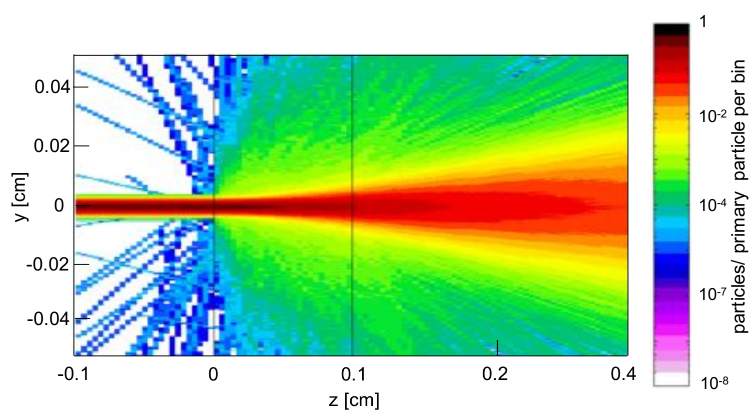

Figure 1.7: FLUKA simulation of a 20 MeV electron beam crossing a 1 mm thick aluminum foil (black lines at 0 and 0.1 cm); the divergence of the beam coming out of the material is 35 mrad root-mean-square (r.m.s.).

Chapter 2

Theoretical background

2.1 Plasma wakefield theory

2.1.1 Definition of plasma

Plasma is a state of matter in which long-range electric and magnetic fields dominate the behaviour of the matter. To fullfill the definition of a plasma, three properties must be satisfied [26]:

1. Quasi-neutrality: the number of positive and negative charges is the same, so that the plasma appears neutral from outside. This happens when the Debye length is short compared to the physical size of the plasma. The Debye length λ_{D} is defined as:

$$\lambda_{\mathrm{D}} = \sqrt{\frac{\epsilon_0 T_{\mathrm{e}}}{n_{\mathrm{pe}} e^2}}, \tag{2.1}$$

   where ϵ_0 is the vacuum permittivity, T_e is the plasma electron kinetic temperature, n_{pe} is the plasma electron density, and e is the elementary charge.

2. Collective behaviour: the number of particles N_D within a Debye sphere (a sphere whose radius is the Debye length) is much larger than one. If a plasma has much more than one particle in a Debye sphere, charges interact with many nearby charges; consequently, plasma waves can exist as a result of the collective response of the plasma. The electrostatic potential of a particle outside of the sphere on a given charge is shielded as $e^{-\lambda_D r}$, which is much shorter than $\frac{1}{r}$ outside a plasma.

3. The plasma electron frequency ω_{pe} is larger than the electron collision frequency. ω_{pe} is defined as:

$$\omega_{\mathrm{pe}} = \sqrt{\frac{n_{\mathrm{pe}} e^2}{\epsilon_0 m_{\mathrm{e}}}}, \tag{2.2}$$

where m_e is the electron rest mass. If this property is satisfied, electrostatic interactions dominate over ordinary gas kinetics as well as over collisions.

2.1.2 Beam-driven plasma wakefield generation

When a highly relativistic bunch of charged particles (the *driver*) travels into an initially neutral plasma, its beam charge density n_b generates a space-charge potential that displaces plasma electrons; heavy (and thus immobile on the timescale of ω_{pe}) plasma ions provide a restoring force that leads to a plasma electron density oscillation [27]. The plasma wake oscillates at the plasma electron frequency ω_{pe} and follows the drive bunch similarly to water wakes following a fast boat.

Plasma wakefield theory [28] shows that a charged particle bunch induces an electrostatic plasma response. The resulting plasma wave has radial (periodically focusing and defocusing) and longitudinal (periodically accelerating and decelerating) components. The radial and longitudinal fields are $\lambda_{\mathrm{pe}}/4$ out of phase. The wave travels with a velocity v_{ph} approximately equal to the drive beam velocity v_b.

The longitudinal component of the electric field E_z (in the direction of the wave-vector) can be used to accelerate charged particles. Transverse components (both electric and magnetic) generate focusing and defocusing forces. Figure 2.1 shows the charge separation as well as the plasma wakefields generated by a positive charged driver: the arrows correspond to regions of focusing (green), defocusing (red), accelerating (orange) and decelerating (purple) wakefields for negatively charged particles.

In the linear regime ($n_b << n_{pe}$), the conditions for the most effective wakefield excitation by a Gaussian drive bunch with r.m.s. length σ_{z} and r.m.s. transverse size σ_{r} are [29]:

$$\sigma_{\mathrm{z}} \simeq \frac{\lambda_{\mathrm{pe}}}{\sqrt{2}\pi}, \tag{2.3}$$

where λ_{pe}=2πc/ω_{pe} (c is the speed of light) is the plasma electron wavelength, and

$$\sigma_{\mathrm{r}} \simeq \frac{\lambda_{\mathrm{pe}}}{2\pi} = \frac{c}{\omega_{\mathrm{pe}}}, \tag{2.4}$$

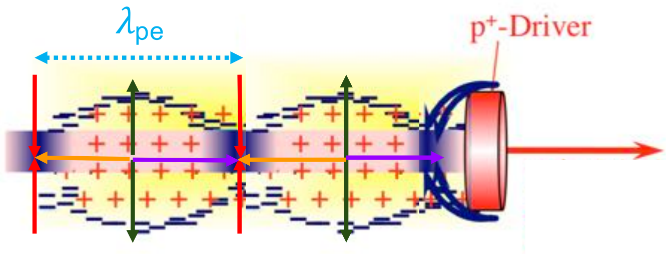

Figure 2.1: Schematic drawing of the charge separation generated by a proton bunch travelling in a plasma. '-' are the plasma electrons, '+' are the heavy plasma ions. The scheme also shows the non-linear fields sustained by the charge separation.

i.e. the drive bunch length is on the order of half the plasma electron wavelength and the beam size is transversely almost equal to the collisionless plasma skin depth c/ω_{pe}. If the drive bunch and the plasma fulfill these conditions, plasma wakefield theory [29] indicates that the amplitude of the accelerating field can be estimated by $E_{acc}= (n_b/n_{pe})\ E_{wb}$, where E_{wb} is the cold-wavebreaking non-relativistic plasma field (called E_{max} in Equation 1.1), defined as:

$$E_{\rm wb} = \frac{m_{\rm e} \cdot c \cdot \omega_{\rm pe}}{e}. \tag{2.5}$$

2.1.3 The AWAKE plasma and wakefields

The AWAKE plasma is created by ionizing rubidium vapor [30] with a $\sim$ 100 fs and $<$ 450 mJ laser pulse focused to $r \approx$ 1 mm at the plasma entrance. With these parameters, the focused laser pulse intensity and energy are high enough to ionize the outermost electron of each rubidium atom (ionization potential is 4.12 eV) [31]. Both electrons and ions are present in the plasma, hence the plasma is quasi-neutral.

AWAKE uses the transverse fields of a relativistic (γ=427) proton bunch to drive wakefields. Highly relativistic proton bunches carry almost purely transverse electric fields. When the proton bunch drives plasma wakefields, part of the energy stored in the bunch can be converted into a longitudinal electric field that can be used for charged particle acceleration (orange arrows in Figure 2.1).

The AWAKE baseline plasma electron density is chosen to be $7{\cdot}10^{14}$ electrons/cm^3 based on the radial proton bunch size at the plasma entrance ($\sigma_{\rm r} \sim 0.2$ mm) so as to satisfy Equation 2.4. To fulfill both conditions for effective wakefields excitation, the bunch should have a length on the order of $\lambda_{\rm pe} = 1.2/\sqrt{2}\pi$ mm. Unfortunately, the proton bunch delivered by the CERN SPS has a length on the order of $\sim 6-12$ cm, which is too long to generate high amplitude wakefields at these plasma electron densities. Hence, to create an accelerating field strength on the order of GV/m, the AWAKE experiment relies on the development of a process called the seeded self-modulation (SSM) [14]: the transverse wakefields generated by the head of the bunch modulate the trailing part of the bunch into micro-bunches spaced at the plasma wavelength $\lambda_{\rm pe}$. These micro-bunches then satisfy both conditions of Equations 2.3 and 2.4 and, since they are spaced of $\lambda_{\rm pe}$, they resonantly drive wakefields.

In 2016 and 2017 (Run 1-Phase 1), AWAKE observed the self-modulation of the proton bunch, as well as its growth along the plasma [32][33] and along the bunch [34].

To avoid defocusing of the witness electron bunch in the beginning of the plasma, electrons are injected obliquely into the plasma (see Figure 2.2). They cross the wakefields at a certain distance inside the plasma, where the wakefield phase does not evolve strongly anymore and wakefields evolved to include defocusing regions also in the beginning of the bunch [24][25].

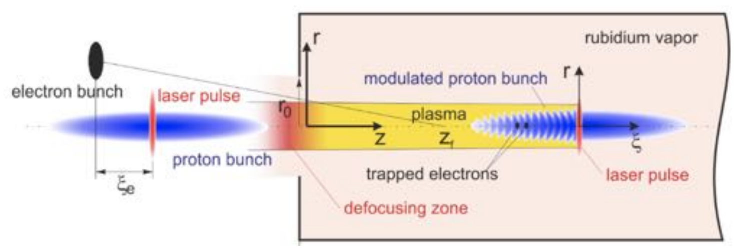

Figure 2.2: Schematic drawing of the witness injection scheme. The electron bunch (black) is obliquely injected into the plasma so as to cross the proton bunch (blue) only once the wakefield phase does not evolve strongly anymore (at $n_{\rm pe} = 7 \cdot 10^{14}\,{\rm cm}^{-3}$, SSM saturation occurs at z$\sim$ 4 m, at $n_{\rm pe} = 2 \cdot 10^{14}\,{\rm cm}^{-3}$, at z$\sim$ 6 m). We notice that the laser pulse (red) is located in the middle of the proton bunch in time, so the first half of the bunch doesn't propagate in plasma, but in the rubidium vapor.

In AWAKE Run 1, the electron bunch length is on the order of the plasma wavelength (so as to maximize the probability of charge capture without a synchronization precision $< \pi/2\omega_{\rm pe}$). Some electrons will be reflected by the defocusing fields as soon as they enter the plasma. For this reason, I expect to observe increased electron losses on the BLM system downstream the injection point during the acceleration experiment.

2.2 Particle-matter interactions[1]

2.2.1 Electron interaction with matter

An electron passing through matter experiences energy loss (1) and deviation from its initial trajectory (2) due to: inelastic scattering on material's electrons and Coulombian interaction with the nuclei. The material stopping power dE/dx is defined as the amount of energy loss by a particle crossing a material of thickness x. The first process is well described by the *Bethe-Bloch* formula; the second is ruled by the *Bremsstrahlung* process, which causes multiple scattering and thus trajectory deviations.

1. The *Bethe-Bloch* formula describes the mean energy loss through ionization process of particles crossing a material. The specialized formula for electrons is [37]:

$$-(\frac{dE}{dx})_{\mathrm{ionization}} = 4\pi N_{\mathrm{A}} {r_{\mathrm{e}}}^2 m_{\mathrm{e}} c^2 \frac{Z}{A}\frac{\rho}{\beta^2}[ln(\frac{\gamma m_{\mathrm{e}} c^2 \beta\sqrt{\gamma-1}}{\sqrt{2}I})+F(\beta)] \quad [\frac{MeV}{cm}]. \tag{2.6}$$

   where N_A is the Avogadro number, r_e is the classical electron radius, m_e is the electron mass, c is the speed of light, Z is the material atomic number, A is the material atomic mass, ρ is the material density expressed in g/cm^3, β and γ are the relativistic factors, I is the material ionization constant, well approximated by: $I = 16Z^{0.9}$ eV, and *F(β)* is a correction factor for light relativistic particles. For electrons *F(β)* is defined as:

$$F(\beta) = \frac{1}{2}(1-\beta^2) - \frac{2\gamma-1}{2\gamma^2}ln2 + \frac{1}{16}(\frac{\gamma-1}{\gamma})^2. \tag{2.7}$$

   The *Bethe-Bloch* formula provides the average energy loss. For materials with a thickness $> 1\,\mathrm{g/cm^2}$, the energy loss has a Gaussian distribution, with a standard deviation σ_0 of:

$$\sigma_0 = \sqrt{4\pi N_{\mathrm{A}} {r_{\mathrm{e}}}^2 (m_{\mathrm{e}} c^2)^2 \frac{Z}{A}\rho} \quad [\frac{MeV}{cm}]. \tag{2.8}$$

[1]The major sources for this section are [35] and [36].

2. Because of the interaction with nuclei electric fields, electrons are steered from their original trajectory. They experience acceleration and therefore emit photons, according to the *Bremsstrahlung* (or *Braking Radiation*) process. Since they emit photons, they also loose energy. This is why *Bremsstrahlung* also contributes to energy losses as following:

$$-(\frac{dE}{dx})_{\mathrm{Brem}} = 4\alpha N_{\mathrm{A}}\rho {r_{\mathrm{e}}}^2 \frac{Z^2}{A} Eln(\frac{183}{Z^{\frac{1}{3}}}) \quad [\frac{MeV}{cm}], \tag{2.9}$$

where α is the fine structure constant and E is the electron energy expressed in MeV. A model developed by Molière predicts the r.m.s. angular spread of the Gaussian core as:

$$\theta_0(x) = \frac{13.6MeV}{\beta cp}\sqrt{x/X_0}[1 + 0.038\ln x/X_0] \quad [rad]. \tag{2.10}$$

where p is the electron momentum (expressed in MeV/c) and X_0 is the material radiation length.

2.2.2 Photon interaction with matter

Photons with a given energy E_γ interact with matter with three main processes: photoelectric effect (1), Compton scattering (2) and pair production (3).

1. During the photoelectric effect, a photon deposits its total energy in a single interaction with an absorber atom; a photoelectron is emitted with the energy E_e=E_γ-E_b, where E_b is the binding energy of the photoelectron. Photoelectric cross-section is proportional to:

$$\sigma_{\mathrm{pe}} \propto \frac{Z^4}{{E_\gamma}^5}, \tag{2.11}$$

and rapidly increases with the material atomic number. This process dominates over the other processes (2,3) at photon energies lower than 100 keV.

2. Compton scattering describes scattering on atomic electrons: the photon is deflected and loses energy. The Compton cross-section scales as:

$$\sigma_{\mathrm{C}} \propto \frac{Z\ln E_\gamma}{E_\gamma}. \tag{2.12}$$

It dominates for a photon energy range between 100 keV and 1 MeV.

3. If the photon energy is equal or more than twice the mass of the electron, an electron-positron pair can be produced (in presence of a nucleus), with no energy losses in the material. The pair production cross-section scales as:

$$\sigma_{\mathrm{C}} \propto Z^2. \tag{2.13}$$

For a given material, it is constant and dominates for $E_\gamma >> 1\,\mathrm{MeV}$.

2.2.3 Expected energy loss for the AWAKE electron beam

The AWAKE electron beam has an energy of $\sim$ 18 MeV, (β $\sim$0.9996 and γ $\sim$35).

The vapor source consists of several layers (see Figure 2.3). Electrons cross three stainless steel cylinders, galden (at 160 - 250°C) and rockwool before exiting the system.

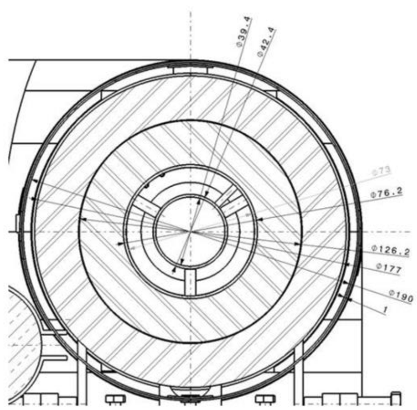

Figure 2.3: Technical drawing of the vapor source (longitudinal cross-section).

For analytical calculations, I approximate the steel layers with iron. I neglect the galden and rockwool layers, since the electron cross section is small compared to the steel alone. Starting from the inner one, the steel layers have a thickness of 1.5, 1.6 and 1 mm. Considering a 18 MeV electron that impacts perpendicularly on the vapor source pipe, I calculated energy loss and scattering angle for each layer (using Equations 2.6, 2.9 and 2.10). Electrons exiting the vapor source have an average energy of (8.6 ± 0.5) MeV and a root-mean-square (r.m.s.) angular deviation from initial trajectory of 44.5 rad.

Furthermore, because of the *Bremsstrahlung* process, X-rays are emitted with energies up to the $-(\frac{dE}{dx})_{\text{Brem}}$ value ($\sim 1\,\text{MeV/c}^2$) (calculated with Equation 2.9). Even though emitted photons are less energetic than electrons, their energy deposition in a detector (see Section 2.3) might be still significant as their angular divergence is small: they are produced in a cone with an r.m.s. spread of $\sim 1/\gamma$ (0.47 rad).

Figure 2.4 shows the iron stopping power for electrons as a function of energy. The iron radiation length X_0 is $13.8\,\text{g/cm}^2$.

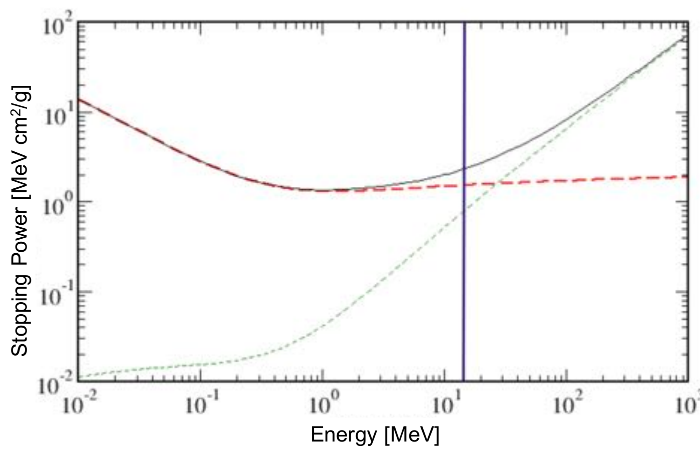

Figure 2.4: Iron stopping power for electrons as a function of their initial energy. Solid black line is the total stopping power, whose two components are the ionization process (red dashed line) and *Bremsstrahlung* (green dashed). The blue vertical line indicates the AWAKE electron beam energy of 18 MeV. At this energy the two components are almost equal.

2.3 Scintillation detectors[2]

To detect electron beam losses, we use organic plastic scintillators positioned along the vapor source. These devices rely on the scintillating property of the active material: as radiation passes through the scintillator, it deposits energy (as explained in Section 2.2) and excites the atoms and molecules of the scintillator, causing light to be emitted. This property is known as *luminescence*. Luminescent materials absorb energy and reemit it in the form of visible light.

[2]The major sources for this section are [36] and [38].

If the reemission occurs immediately after absorption (within $\sim 10^{-8}\,$s) the process is called *fluorescence*. If reemission is delayed because the excited state is metastable, the process is called *phosphorescence*.

The time evolution of the reemission process (shown is Figure 2.5) may be described as a two-component exponential:

$$N(t) = A \cdot exp(\frac{-t}{\tau_{\mathrm{f}}}) + B \cdot exp(\frac{-t}{\tau_{\mathrm{s}}}), \tag{2.14}$$

where N is the number of photons emitted at the time t, τ_{f} and τ_{s} are the decay constants, A and B are normalization factors.

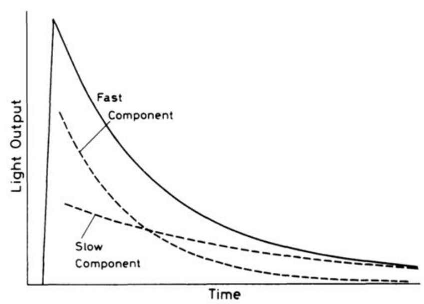

Figure 2.5: Time evolution of the light emission process of an organic scintillator. Dashed lines show the fast and slow components; solid line represents the total light decay curve.

Since one component is generally much faster than the other, I will refer to them as the *fast* and *slow* components. Organic scintillators are:

- sensitive to energy: most scintillators behave almost linearly with respect to the energy deposited, i.e. the light output of a scintillator is directly proportional to the exciting energy;
- fast: response and recovery times are on the order of few nanoseconds;
- highly efficient for conversion of exciting energy to fluorescent radiation (on the order of 10^4 photons per deposited MeV by electrons);
- transparent to their own fluorescent radiation so as to allow transmission of the light;
- resistant to temperatures up to $+60°$C: light output emission is weakly affected.

Organic scintillators are aromatic hydrocarbon compounds containing linked or condesed benzene-ring structures. Scintillation light in these compounds arises from transitions made by the free valence electrons of molecules. These delocalized electrons are not associated with any particular atoms and can occupy spin singlet states (S) or spin triplet states (T). Electrons are normally in the ground states (S_0, T_0); penetrating radiation can excite electrons to higher energy states (S^*, S^{**}, T^*, T^{**}). Also associated with each electron level is a fine structure which corresponds to excited vibrational modes of the molecule. The energy spacing between electron levels is on the order of a few eV, while that between vibrational levels is on the order of a few tenths of eV. An energy diagram for these orbitals is shown in Figure 2.6.

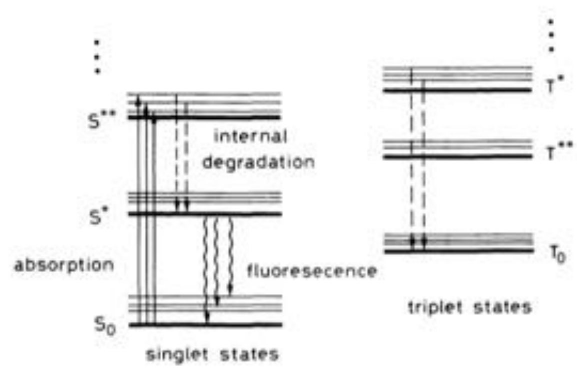

Figure 2.6: Energy level diagram of an organic scintillator molecule. Singlet states (denoted by 'S') are separated from the triplet states (denoted by 'T'). Arrows pointing up show the excitation from the ground state of molecoles due to the energy absorption; arrows pointing down illustrate the deexcitation of molecules via internal degradation (dashed lines) and fluorescence (wavy lines).

The singlet excitation generally decays immediately ($\leq 10\,\text{ps}$) to the state S^* without the emission of radiation (*internal degradation*). From S^*, there is a high probability of making a radiative decay to one of the vibrational states of the ground state S_0 within a few nanoseconds (fast component). The fact that S^* decays to excited vibrational states of S_0 also explains the transparency of the scintillators to their own radiation.

For the triplet excited states, a similar internal degradation process occurs which brings the system to the lowest triplet state. The T_0 state then decays mainly by interacting with another excited T_0 molecule,

$$T_0 + T_0 \rightarrow S^* + S_0 + phonons, \tag{2.15}$$

leaving one molecule in the S^* state. Radiation is then emitted as described above. This light comes after a delay time characteristic of the interaction between the excited molecule and is the slow decay component.

The response of a scintillator is actually a complex function of not only energy but the type of particle and its specific ionization. Assuming the response of organic scintillators to be ideally linear with the deposited energy, the semi-empirical Birk's Law explains the deviations as being due to quenching interaction between the excited molecules created along the path of incident particles. Since a higher ionizing power produces a higher density of excited molecules, more quenching interactions will take place for these particles. The light output per unit of lenght, dL/dx, is thus related to the stopping power for a given species as:

$$\frac{dL}{dx} = \frac{A\frac{dE}{dx}}{1 + B\frac{dE}{dx}}, \tag{2.16}$$

where A is the absolute scintillation efficiency and B is a parameter relating the density of ionization to dE/dx, and they are obtained by fitting experimental data. Hence, for small dE/dx Birk's law reduces to a linear relationship:

$$\frac{dL}{dx} \simeq \frac{dE}{dx}, \tag{2.17}$$

while, for large dE/dx, Birk's formula implies saturation:

$$\frac{dL}{dx} \simeq \frac{A}{B}. \tag{2.18}$$

Furthermore, the overall decay time of the emitted light pulse varies with the type of exciting radiation. Scintillators are thus capable of *pulse shape discrimination*. Figure 2.7 shows the different decay time of stilbene (an organic plastic scintillator similar to polyvinyltoluene) when excited by different particles. The explanation for this effect lies in the fact that the fast and slow components arise from the deexcitation of different states of the scintillator. Depending on the energy loss of the particle, these states are populated in different proportions, so that the relative intensities of the two components are different for different dE/dx.

In conclusion, I expect to observe a different behaviour (in both intensity and timing) of the scintillation light emission for the 18 MeV electrons ($dE/dx \approx$

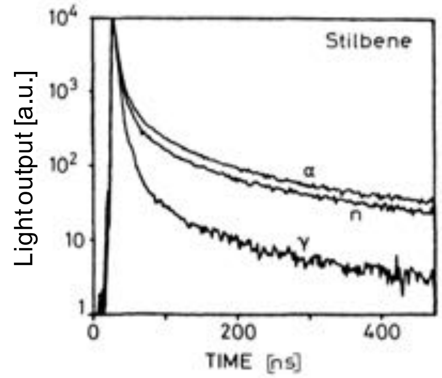

Figure 2.7: Pulse shape of stilbene light for alpha particles, neutrons and gamma rays [38].

2 MeV·cm^2/g) and 400 GeV protons ($dE/dx > 10^4$ MeV· cm^2/g) on the electron beam loss monitors.

2.4 FLUKA simulations of the beam loss monitor setup

To understand loss detection and to prove the feasibility of the beam loss monitor setup concept, I used FLUKA for simulations. FLUKA is a general purpose Monte Carlo simulation package for calculations of particle transport and interaction with matter [39]. The goal is to prove that when the beam is lost on the vapor source's surrounding material, the energy deposited by secondary and scattered particles into simulated detectors is enough to produce a clear signal in a real detector (detection threshold is around 100 keV of deposited energy [40]).

2.4.1 Simulation parameters

I built a model of the AWAKE vapor source (Figure 2.8), approximating stainless steel with iron and galden with water, and positioned detectors along it to measure the deposited energy. Since polyvinyltoluene was not available in the material database of FLUKA, I replaced it with polyethilene (symilar polymer to the real detector material). The detector dimensions are $3 \times 3 \times 0.4\,\text{cm}^3$.

The input electron beam in the simulations is based on the nominal experimental values: transverse r.m.s. beam size $\sigma = 250\,\mu$m, normalized emittance $\epsilon_{\mathrm{N}} = 2\,$mm·mrad, energy E=18 MeV. I simulated different injection schemes: oblique, varying the vertical angle (red arrow in Figure 2.8); parallel to the vapor source (green arrow), varying the vertical offset. In all simulations, the vapor source chamber is considered under vacuum, since the Rb vapor density is $< 10^{15}$ atoms/cm$^3 \simeq 10^{-4}$ bar and thus negligible. Each simulation is made up of five cycles of 10^4 events.

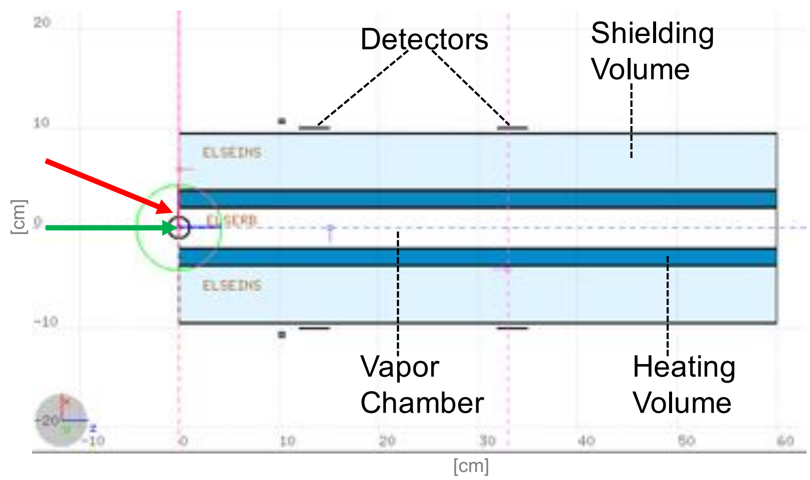

Figure 2.8: Simulated layout of the vapor source in the FLUKA geometry interface (first 60 cm, side view). The inner white cylinder is the vapor chamber (under vacuum in simulations); in blue colors the heating and shielding volumes. Detectors are positioned along the source.

2.4.2 Simulation results

Preparatory studies

I simulated the interaction of the beam with the vapor source. Figure 2.9*a* shows the electron beam impacting on the pipe material. Electrons are scattered at large angles. After interacting with the source's layers, some electrons exit the system and deposit energy in the detectors. I also studied the production and propagation of photons (Figure 2.9*b*) due to the interaction, since photons will also deposit energy in the detector material (as discussed in Section 2.2.2), even if their interaction cross section is small (the energy deposition of a 1 MeV photon is ∼200 times lower than a 8 MeV electron), as their flux intensity is high.

Particularly, they keep the primary beam direction and thus contribute significantly to the energy deposition in the detectors. We note that the number of photons at the detector location (red circles in Figure 2.9) is ∼50 times the number of electrons.

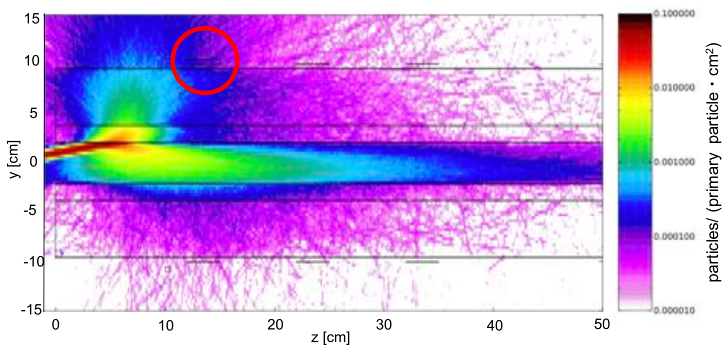

(a) Electrons spatial distribution

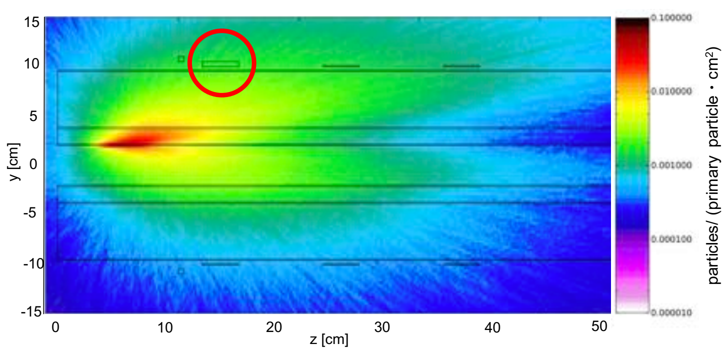

(b) Photons spatial distribution

Figure 2.9: Simulation results for the electron beam impacting on the vapor source. Panel (a) shows the spatial distribution of electrons (primary beam and scattered); panel (b) shows the spatial distribution of produced photons. The detector closest to losses location is marked with a red circle.

Oblique injection scheme

I simulated the injection of the beam into the vapor source varying its vertical injection angle from 0 to 8 mrad, in 1 mrad steps. These simulations study the injection scheme in plasma wakefields when the electron beam misses the wave and propagates straight on its initial trajectory. Figure 2.10 shows the deposited energy for the detector positioned below the vapor source for an injection angle of 6 mrad pointing down. Assuming that real detector material has a scintillation efficiency of 10^4 photons/MeV [41] and a threshold of detection around 100 keV of deposited energy [40], and that the electron beam consists of $\sim 10^9$ particles, scintillators will produce a detectable loss signal. The highest deposit takes place in the detectors close to the position where the beam is lost. The real detectors will be positioned at least 1 meter apart from each other, thus the spatial resolution of this measurement will be given by the detector spacing.

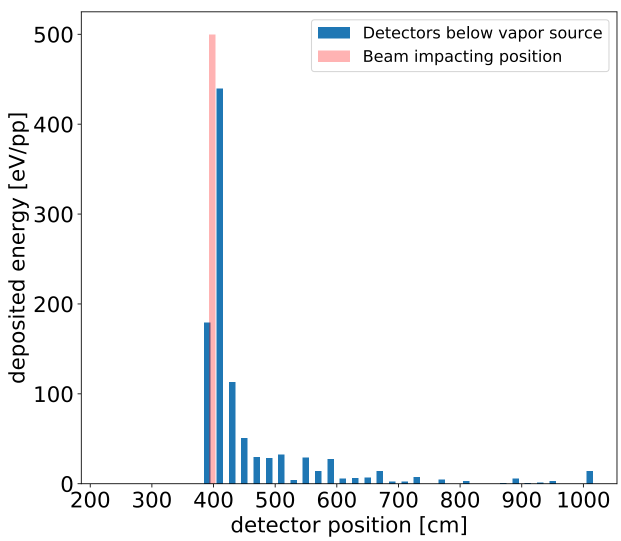

Figure 2.10: Deposited energy for different detectors positioned below the plasma source for a vertical injection angle of 6 mrad pointing down. The red bar shows the position where the primary electron beam impacts on the vapor source inner layer. Deposited energy is expressed in eV per primary particle.

Parallel injection scheme

I then studied the situation where the electron beam impacts on the aluminum entrance layer of the source. To focus only on this phenomenon, I simulated an electron beam that propagates parallel to the vapor source and impacts on the entrance at different vertical positions (between -1.8 and 1.8 mm in 20 steps). Figure 2.11 shows the simulation results for the beam hitting the layer at vertical offset y=1 cm for different detector positions along the plasma. We note that the highest energy deposition takes place for detectors positioned

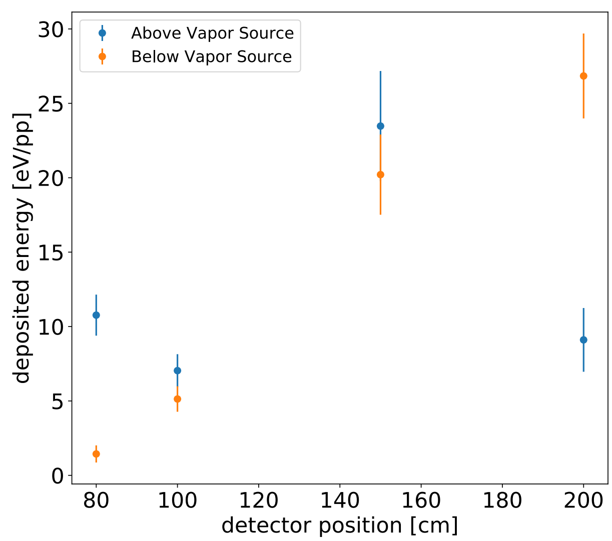

Figure 2.11: Deposited energy for different detectors positions along the plasma source, simulated on top of (blue dots) and below (orange dots) the plasma source. Primary electrons hit the entrance layer at vertical offset y=1 cm. Errorbars are the standard errors.

at least 150 cm downstream the entrance. This observation can be explained considering that beam emittance blows up because of the interaction with the entrance layer; therefore, particles start diverging with a small angle, going to impact on the pipe about 1.5 m downstream. Hence, I considered 150 cm downstream the entrance the lower distance limit for the installation of the real detectors. Additionally, to be able to detect losses on both sides of the vapor source for all impact offset on the entrance layer, I considered 150 cm the best position because it maximizes the deposited energy for both detectors.

Figure 2.12 shows the energy deposition in the detector 150 cm downstream the entrance, above the vapor source, as a function of the vertical offset of the beam at the entrance aperture location. Between ~ -0.5 and ~ 0.5 cm, there are no losses, as the beam completely passes through the entrance and doesn't interact with the iris. After increasing the offset absolute value, the energy deposition increases, saturating around an absolute vertical offset of 1.6 mm.

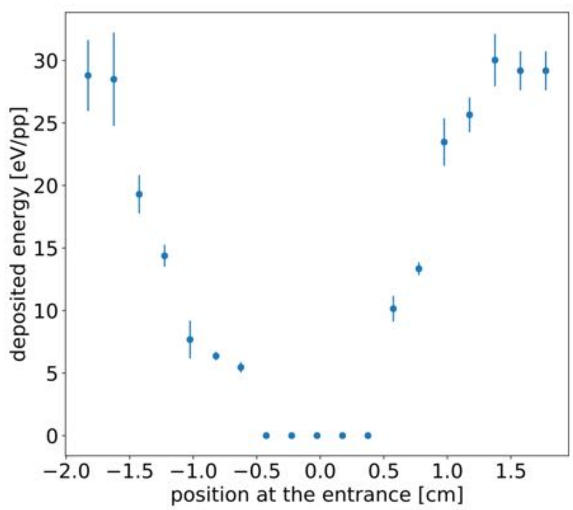

Figure 2.12: Deposited energy as a function of the beam vertical offset in the detector positioned 150 cm downstream the entrance, above the vapor source. Errorbars are the standard errors.

Thus, detectors positioned at this distance from the entrance will be able to tell when the beam (or a part of it) interacts with the entrance layer. We note that the distribution is not as symmetric as expected, due to simulation uncertainties caused by the limited number of events.

2.4.3 Conclusions

Primary electron beam interacts with the vapor source and produces scattered electrons and photons. These secondaries can exit the vapor source system and their energy deposition in a detector is above the detection threshold. From FLUKA simulations we learned that the spatial resolution, determined by the detector spacing, allows to estimate where the beam is lost (on the meter scale) and whether it interacts with the aluminum entrance layer.

2.5 Electron beam transfer line optics

The electron bunch is produced by an electron photo-injector with an output energy of 5 MeV and accelerated to 10 − 20 MeV in a 1 m long booster structure. Electrons are transported from the electron source to the rubidium vapor source by a 15 meter long transfer line (the general layout is shown in Figure 2.13). The electron beam trajectory is steered both vertically and horizontally with large angles: thus dispersion contributes to the transverse beam size along the transport (see Figure 2.14).

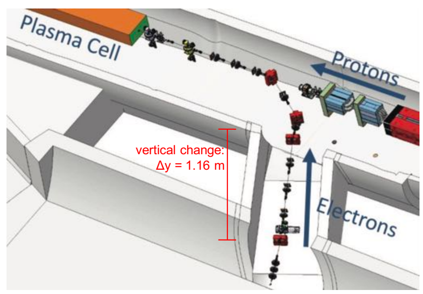

Figure 2.13: View of the AWAKE electron transfer line. Electrons are horizontally and vertically steered to merge trajectory with protons to be injected in the plasma.

2.5.1 Transverse electron beam size

For a beam of a given geometric emittance ϵ, the transverse r.m.s. beam envelope evolves as [7]:

$$\sigma_{\mathrm{x,y}} = \sqrt{\epsilon_{\mathrm{x,y}}\beta_{\mathrm{x,y}} + D_{\mathrm{x,y}}\delta}, \tag{2.19}$$

where β is the so-called beta-function, D is the dispersion and δ is the beam momentum spread $\delta{=}\Delta p/p$ (p is the beam momentum). According to the theoretical optics and simulations [42] (Figure 2.14 shows MadX simulation of the beam line optics), the dispersion is on the order of few cm and $\beta \sim 1\,\mathrm{m}$ at the focal point. Therefore, the beam has its smallest transverse size and a

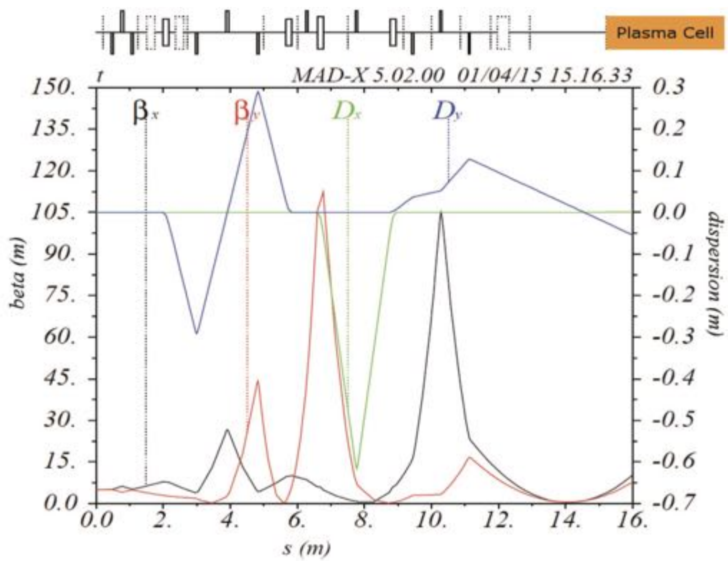

Figure 2.14: MadX simulation results showing the β-function and the dispersion along the electron beam line for a focal point positioned $\sim 2\,\mathrm{m}$ upstream of the vapor source entrance.

round shape at the focal point, while far away from the focus the transverse size increases and, since D_x, $D_y \neq 0$ and $D_x \neq D_y$ the beam shape is not round.

Measuring the electron transverse beam size at the plasma entrance, I thus expect to observe minimum round size when the beam is focused at the aperture and bigger not-round size when the beam is focused further downstream.

The electron beam source can provide an electron beam charge between 0.1 and 1 nC [43]. Because of the larger laser spot on the source cathode for higher UV-laser energies, and due to space-charge effects, the transverse emittance of the beam increases with the charge. We measure normalized emittance ϵ_{N} for 200 and 600 pC beams (using a *Pepper-pot* screen [44]) to be ~ 4 and 8 mm·mrad respectively. Consequently, according to Equation 2.19, the transverse beam size will be different for the two beams. Since the optics of the line doesn't change with the electron bunch charge, and the beam transport is insensitive to initial conditions [45], focusing the beam at the entrance, I expect to measure $\sigma_{600} \sim \sqrt{2}\sigma_{200}$, where σ_{200} and σ_{600} are the transverse r.m.s. beam size for the 200 and 600 pC beam respectively. Moreover, focusing the beam further downstream, I expect σ_{600} to increase more with respect to σ_{200} because of the larger energy spread of the 600 pC bunch (the higher charge beam is longer because of space charge effects, thus the beam energy spread out of the booster is higher).

2.5.2 Earth magnetic field effect on the beam trajectory

Electrons have a longitudinal momentum of $\sim 18\,\mathrm{MeV/c}$ and the beam electron transfer line is not and cannot be shielded from external magnetic fields (shielding of the line was technically too challenging within constraints). The earth magnetic field B ($\mathrm{B_x} \sim 0.4\,\mathrm{Gauss}$, $\mathrm{B_y} \sim 0.2\,\mathrm{Gauss}$, corresponding to a Larmor radius $r_L = \beta\gamma m_e c/eB$ of ~ 1.5 and $3\,\mathrm{km}$, respectively) leads to a significant electron deflection angle (see Figure 2.15). Particularly, the beam trajectory between the last magnetic element and the entrance of the vapor source (more than 3 meters) cannot be considered straight: the earth magnetic field bends the beam onto a circular trajectory. The vapor source, on the other hand, is shielded by mu-metal. Thus, inside the source, the electron beam trajectory is straight.

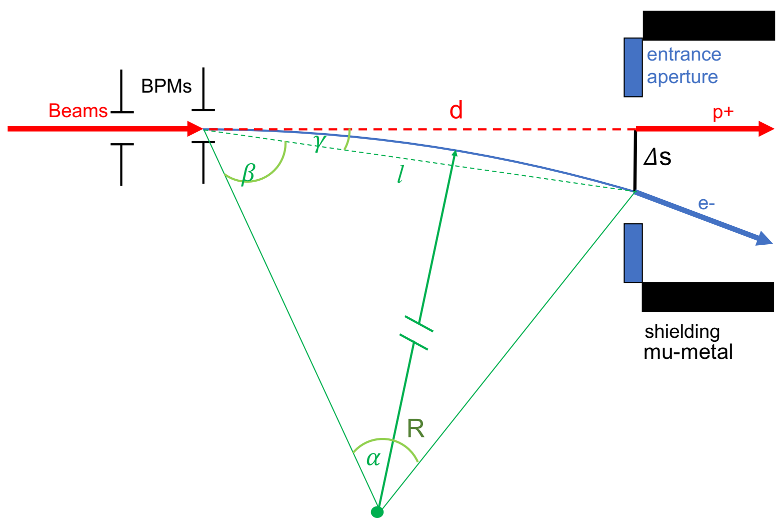

Figure 2.15: Schematic drawing of the trajectory deflection. Beams are aligned in position and angle at the last two BPMs. The proton beam propagates straight (red arrow); the electron beam (blue) is bent by the earth magnetic field. The drawing is not to scale.

Referring to Figure 2.15, I theoretically estimated the deviation of the electron beam from a straight trajectory as:

$$\Delta s = l \sin \gamma. \tag{2.20}$$

The distance l can be in good approximation considered $\sim d$, since propagation distances are on the meter scale and the transverse deflection on the mm scale. After considerations on isoscele triangles, γ=$\alpha/2$. Since α <<1, it can be approximated as $\alpha \sim l/R$. Hence, Equation 2.20 yields

$$\Delta s \sim d \sin(\frac{1}{2}\frac{l}{R}). \tag{2.21}$$

Spatial electron, proton and laser beam alignment is one of the crucial issues of the experiment (see Section 1.2.4), since the transverse extend of the plasma ($\sim$ 1 mm) and wakefields ($\sim$ 0.2 mm) is small. Therefore, we are interested in quantifying the deviation caused by the earth B-field in order to precisely overlap the beams. According to Equation 2.21, I expect to measure a position discrepancy from a straight trajectory prediction at the entrance aperture of 1.3 mm to the right in the horizontal plane, and 0.66 mm pointing down in the vertical plane.

2.6 Conclusions

In this Chapter, I give an introduction to plasma wakefield theory and explain the possibility of proton driven plasma wakefield electron acceleration in the context of AWAKE.

I summarize the interactions of electrons and photons with matter and discuss the properties of scintillation detectors and their application as beam loss monitors in AWAKE.

I present simulation results of the BLM setup, proving its applicability in the experiment and estimating its precision.

I finally present the AWAKE electron transfer beamline and discuss some properties of its transverse optics. I then calculate the deflection of the electron beam trajectory caused by the earth magnetic field.

Chapter 3

Diagnostics setup and measurement concepts

3.1 The electron beam loss monitors

3.1.1 Setup

I installed seven beam loss monitors (BLMs) along the vapor source as schematically shown in Figure 3.1. Two detectors (1,2) are positioned close

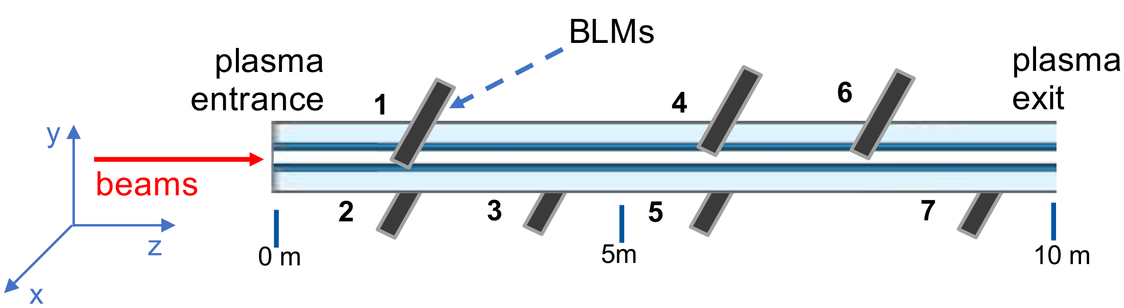

Figure 3.1: Schematic layout of the BLMs setup along the vapor source. The inner white cylinder is the vapor chamber; in blue colors, heating and shielding volumes. Detectors (BLMs) in black. The detector numbers are listed in Table 3.1.

to the entrance aperture, to conduct studies on losses at the entrance. The

Detector number	Distance from the entrance	Relative position w.r.t. the source
1	1.5 m	above
2	1.5 m	below
3	4 m	below
4	6 m	above
5	6 m	below
6	7 m	above
7	9 m	below

Table 3.1: Overview of the BLM detectors numbers and their position along the plasma

other detectors (3, 4, 5, 6, 7) are further downstream, providing information on beam propagation and losses during the injection experiment. Table 3.1 gives the distance from the vapor source entrance aperture and the relative position of each detector. Electronics and power supplies are installed in a radiation-shielded area ~ 100 meters away from the vapor source (see Figure 3.2).

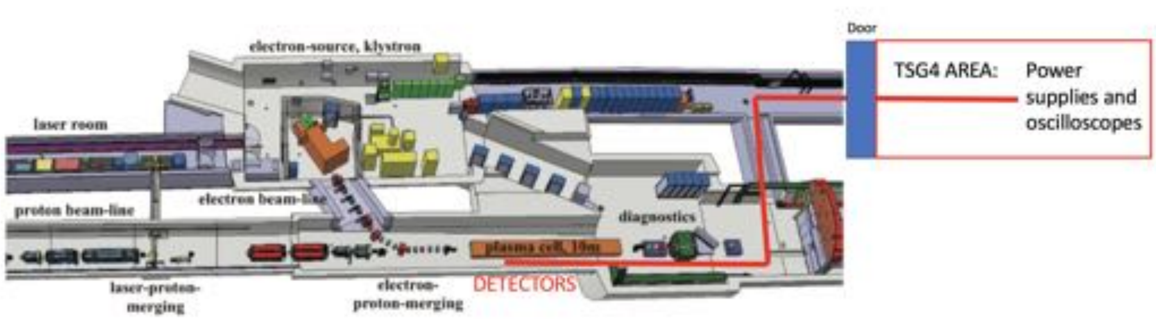

Figure 3.2: The AWAKE experimental area. In red, the cable path connecting detectors (close to the plasma cell) to the electronics read-out and powering.

Each detector (see Figure 3.5a) is ~ 50 cm long and 8 kg heavy. Since the vapor source is positioned at ~ 1.5 m above floor level, scintillators are mounted on aluminum structures (Figure 3.3). Moreover, the active material is oriented parallel to the cell in order to maximize the solid angle for losses detection and to minimize the area exposed to background (see Section 3.2). The final

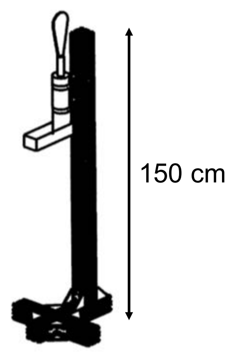

Figure 3.3: Drawing of the aluminum support structure holding one beam loss monitor.

installation of the BLMs in the experimental area is shown in Figure 3.4.

3.1.2 Beam loss monitors working principle

Each detector consists of three main parts (see Figure 3.5*a*):

1. The scintillating material (EJ-200: a polyvinyltoluene based plastic organic scintillator);
2. A photomultiplier (PMT);
3. A light guide optically connecting the two first parts.

When particles deposit energy in the scintillating material, light is produced (as explained in Section 2.3). The emitted light is then collected and transferred to the PMT through the light guide. Photons reaching the PMT hit a photocathode that converts them in electrons via photoelectric effect. Electrons are then accelerated to a series of dynodes, producing more electrons at every stage (sketched in Figure 3.5*b*). Finally, the electron avalanche is collected by an anode providing the signal to the read-out chain. PMTs are powered with a negative high voltage (∼kV) feeding tension to dynodes via a voltage divider.

The voltage signal is read out and digitized by an oscilloscope ($PicoScope$6000) that is remotely connected to a computer where signals are stored. Signal cables (CB50) connect the detectors and the oscilloscopes (the cable impedance is $50\,\Omega$). According to Ohm's law, the integral of the signal is proportional to the amount of charge produced by the PMT, which depends on

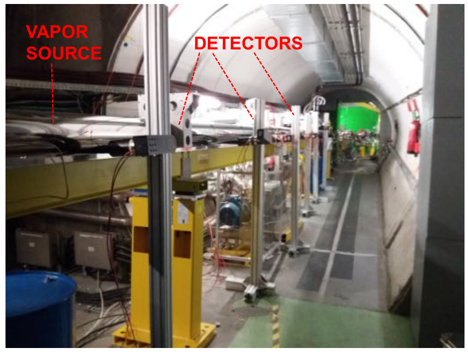

(a) View of the experimental area from the downstream part of the vapor source. The vapor source and the detectors are marked.

(b) Detail of the two detectors close to the upstream entrance aperture. The upstream expansion volume is marked.

Figure 3.4

the energy deposited in the scintillating material (if scintillators and the dynodes are operating in the linear regime). Therefore, the integral of the output signal is proportional to the deposited energy in the scintillator. In the following text, integral output value will be indicated as *counts* and will be expressed in

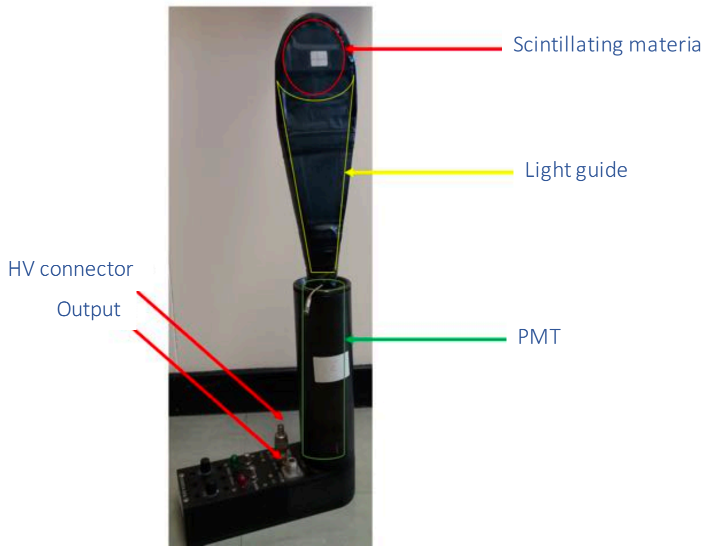

(a) Beam loss monitor before installation; main components are highlighted.

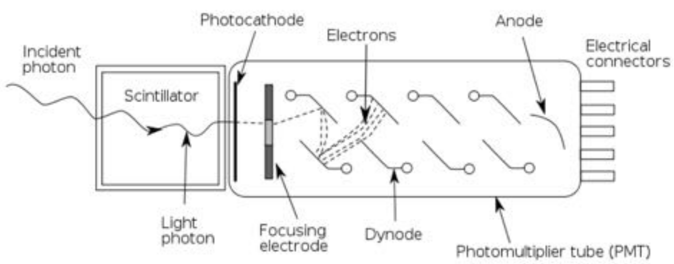

(b) Schematic of the photomultiplier and of its functioning: incident photon is converted into an electric signal amplified by a series of dynodes. Final signal is collected at the anode.

Figure 3.5

arbitrary units ($a.u.$). The error on a single measurement is given by the oscilloscope reading precision. For the $\pm 500\,\text{mV}$ scale, the error on a single sample is $V_{\text{err}} = \pm 4\,\text{mV}$; for the $\pm 1\,\text{V}$ scale, it is $V_{\text{err}} = \pm 10\,\text{mV}$. Hence, for an integration of n samples, the total error is $V_{err}\sqrt{n}$.

To assure that all connections and devices work properly and that long cables can transmit the signal without distortion and losses, I conducted a functioning test on the setup relying on energy deposition from cosmic rays. The PMTs were powered by negative tensions (variable between -1.8 and $-1.5\,\text{kV}$). Figure 3.6 shows the signal generated by a cosmic ray read out by one detector. The signal is well defined and clearly visible above the electronic background noise. As mentioned in Section 2.3, the light emitted by plastic scintillators has a short decay time, usually on the order of few ns. Cosmic ray events allowed me to study the response of the setup for a single-particle event. Hence, I fitted the decay part of the output signal $V(t)$ with an exponential function:

$$V(t) = V_0 \cdot e^{-(t-t_0)/\tau}, \tag{3.1}$$

where V_0 is the minimum of the signal, t_0 is the instant such that $V(t_0)=V_0$ and τ is the decay time. In Figure 3.6 the fit (orange curve) for the early part

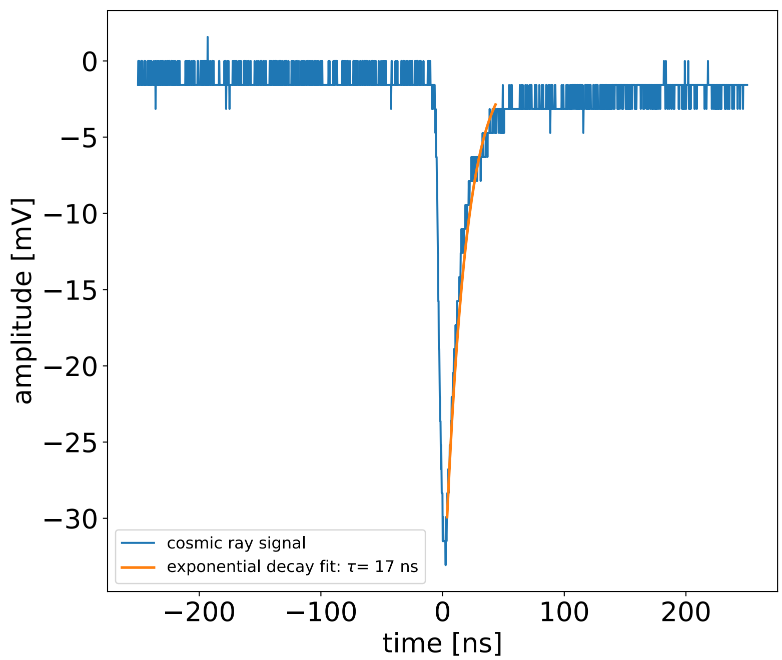

Figure 3.6: A BLM signal generated by a cosmic ray event. Orange line shows the fit of the fast component of the decay signal.

of the decay (fast component) is shown; in fact, the later part is governed by a longer decay time. The result is $\tau = 17\,\mathrm{ns}$. It is higher than the nominal decay time for the scintillator ($2.1\,\mathrm{ns}$ [41]). I suspect that this increase of the decay time may be due to the electronics and/or the long signal cable.

Cosmic rays and background environmental radiation are negligible during the experiment with beams because the PMTs power is lowered (to avoid saturation effects) and because the data-acquisition system is triggered by an external clock signal synchronized with the main laser and the SPS machine.

3.2 Background measurements

Figure 3.7 shows the analogue signals generated by one beam loss monitor in presence of protons (orange line) and electrons (blue) with plasma, and when no beam is present (green). As explained in Section 3.1.2, the signals are processed considering their integral over time.

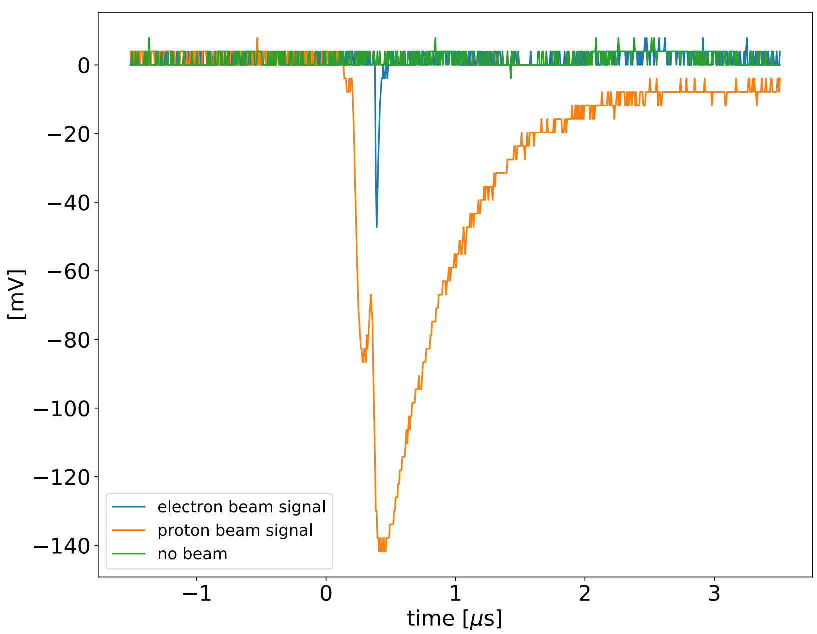

Figure 3.7: Signals generated by an electron beam loss monitor for electrons (blue), protons (orange), or no beam (green), in presence of plasma.

We want to use the BLM setup to conduct measurements on the electron beam when:

1. only electrons are present;
2. in presence of protons.

3.2.1 Measurements without protons

The source of background for measurements with only the electron beam is the electronic noise of the system, but the signal to noise ratio is high enough to always detect the presence of the beam. The background is furthermore minimized reducing the range of integration around the signal spike (between 300 and 500 ns).

3.2.2 Measurements with protons

For measurements in presence of protons, the signal to noise ratio is indeed very small (see Figure 3.7): the maximum amplitude of the proton signal is ~ 3 times higher than the electron's and the integral over the whole signal is ~ 100 times bigger. Therefore, background generated by the proton bunch must be carefully studied and subtracted.

The 400 GeV proton bunch is delivered by the CERN Super Proton Synchroton (SPS). It has a population of $3{\cdot}10^{11}$ particles per bunch and a nominal transverse r.m.s. beam size σ of $\sim 200\,\mu$m at the plasma entrance (see Table 1.1). Sources of background related to the proton beam are two. The first is a safety vacuum separation window between the SPS transfer line and the AWAKE beamline positioned ~ 26 m upstream of the entrance of the vapor source. This is a curved aluminum foil 0.2 mm thick at its center. The interaction of the beam with the separation window generates scattered and secondary particles (most of them in the forward direction). These secondaries can interact with material in or after the plasma section creating background not only for the BLMs but also other diagnostics (e.g. screens). Figure 3.8 shows the results of a FLUKA simulation considering the proton bunch hitting the aluminum window. We note that the total flux of secondary particles at the plasma entrance is high compared to the electron beam intensity (red circle in the plot), and that some particles have very high energy (up to 400 GeV).

The second source of background is the halo of the proton bunch (see Figure 3.13): the distribution of its tails (more than 5 mm apart from the center) does

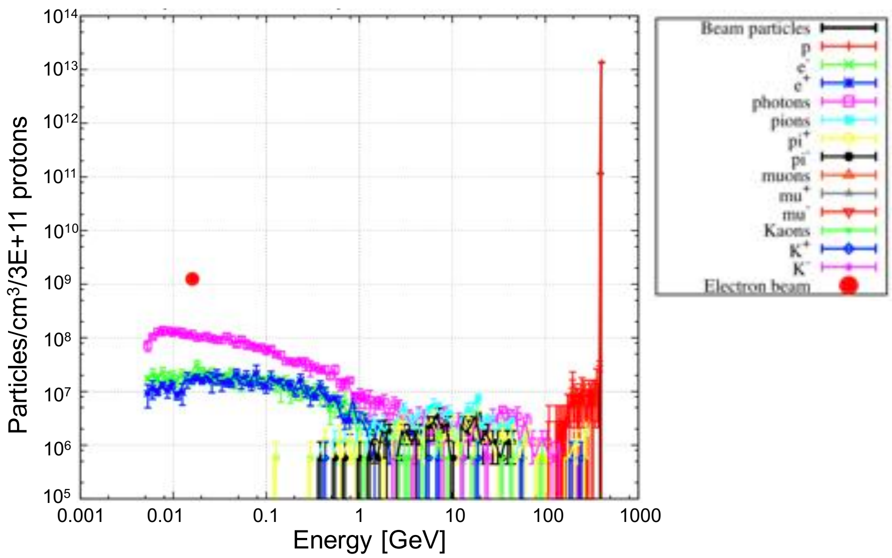

Figure 3.8: Simulated secondary particles spectrum at the plasma source entrance generated by the proton bunch interacting with the separation window.

not correspond to a Gaussian distribution. This non-Gaussian part of the bunch contributes to the background generated by the proton beam. These protons have a trajectory almost parallel to the vapor source and can interact with the beam pipe or diagnostics (e.g. BPMs) and thus produce secondary particles and deposit energy.

As shown in Figure 3.7, the scintillating light emission has different decay times for electrons or protons; in fact, as mentioned in Section 2.3, light emission and decay time of scintillators depends on the ionizing power of the incident particle. To reduce the background signal, we considered only the time range where electron-related signals typically occur, by selecting an integration time-window ($370 - 470\,$ns).

3.2.3 Detector response

The background shower intensity and spatial distribution depend on the proton bunch characteristics (such as length, size, intensity, etc.) and changes on an event-to-event basis. As a consequence, the proton background signal also shows dependencies on these parameters. Particularly, the most significant dependency is on the proton bunch population: the more intense is the primary beam, the more background.

For characterizing this dependency, we collected and integrated over the limited region ($370 - 470\,\text{ns}$) the BLMs signals while varying the proton bunch population from 10^{11} to $3{\cdot}10^{11}$ particles per bunch, and linearly fitted the resulting distribution for each detector. Figure 3.9 shows the distribution and the linear fit for the detector positioned 6 m downstream the plasma entrance, below the vapor source.

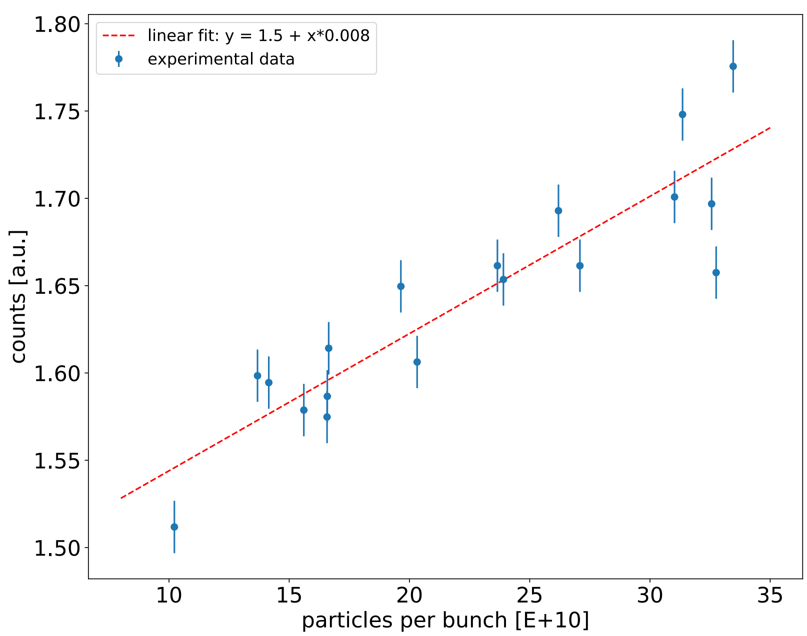

Figure 3.9: Integrated signal over the limited region ($370-470\,\text{ns}$) as a function of the proton bunch population for the detector positioned 6 m downstream the entrance, below the vapor source. The dashed red line shows the linear fit. Errorbars show the intrinsic measurement uncertainty.

The slope of the fit is different for each detector, because they slightly differ from each other (active material efficiency, coupling with the light guide, dynodes amplification, etc.). We note that the response of the detection system is linear as a function of the deposited energy in the active material. During the experiment, the proton bunch population is measured for each event. This allows us to reconstruct and subtract the expected background level.

3.3 Transverse beam size measurements

As mentioned in Section 1.2.4, the vapor source entrance aperture is made of a 600 μm thick aluminum foil and it has a 1 cm diameter opening aperture at its center (see the front view of the plasma source in Figure 1.5*b*). If particles hit the entrance aperture, they interact with the aluminum entrance foil and produce secondary particles. The secondary particles then interact with the surrounding material of the vapor source, increasing the amount of secondaries, and deposit energy in the beam loss monitors (Figure 3.10). Loss signals are approximately proportional to the amount of beam hitting the layer.

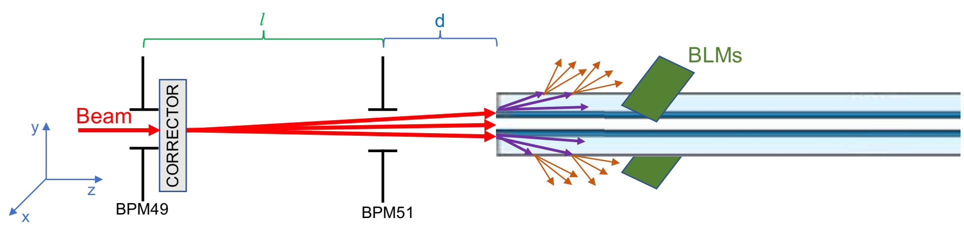

Figure 3.10: Electron beam transfer line and vapor source schematics close to the plasma entrance. Red arrows indicate examples of electron trajectories. Purple and orange arrows indicate secondary particle showers produced when the primary beam interacts with material.

We use the last corrector magnet in the beamline to scan the electron bunch position horizontally and vertically across the entrance aperture, while recording the signals of the electron beam loss monitors close to the entrance (1.5 m downstream, above and below the source), and the horizontal and vertical beam positions measured on beam position monitors BPM49 and BPM51. From this position measurements, we are able to reconstruct the horizontal and vertical (x,y) position of the electron beam at the entrance location using a linear trajectory prediction:

$$(x, y) = \frac{BPM51(x, y) - BPM49(x, y)}{l} \cdot d + BPM51(x, y) \quad [mm], \tag{3.2}$$

where *BPM51* and *BPM49* are the beam position measurements (offset from the center of the beamline expressed in mm), l is the distance between the two BPMs (in meters), and d is the distance between BPM51 and the plasma entrance (in meters). BPM49 is actually positioned upstream the corrector magnet, but we use its measurement as the beam position at the exit of the corrector. In fact, since the two instruments are very close together and the deflection angles are small, we can neglect the effect of the corrector on the beam position and only consider the change on the trajectory angle. We also neglect the effect of the earth magnetic field on the straight trajectory (see Section 2.5.2), since it gives a constant deflection and is thus not relevant for beam size measurements. For each electron beam position, we collect and average 20 measurements. Counts are normalized (to 100 %) to the overall maximum of all measurements in one scan.

Since loss signals are proportional to the amount of the electron beam interacting with the entrance aperture (measured for each position), the result of a scan is the integral of the beam charge intensity distribution over the scanned plane. A complete scan runs from one edge of the entrance aperture to the other, therefore each scan has two ramps (where losses increase from their minimum to their maximum value).

Since the transverse beam distribution is Gaussian, we fit loss signals with error functions to infer the transverse r.m.s. beam size σ at the aperture location. To determine the transverse beam size, both rise ramps are fitted by error functions $erf(\frac{x-\mu}{\sqrt{2}\sigma})$, where μ is the center and σ the standard deviation of the Gaussian distribution. The *erf(x)* is defined as:

$$erf(x) = \frac{2}{\sqrt{\pi}} \int_0^x e^{-t^2} dt. \tag{3.3}$$

The r.m.s. transverse beam size σ is then defined as the average of the two fit results and the uncertainty is calculated from the standard deviation. We measured the transverse beam size for different electron bunch populations and focal point positions (see Section 4.1).

3.3.1 Transverse beam distributions and uncertainties of the measurement

To fit loss signals with error functions, we assume the beam distribution to be transversely Gaussian. To confirm this assumption for the electron beam, we measured its transverse distribution on a scintillating screen close to the entrance (0.8 m upstream). Figure 3.11*a* shows an image of the electron beam on the screen, when the focus is set at the screen location. Horizontal and vertical projections are fitted with Gaussian functions: we note the good agreement between projections and the Gaussian fit. Figure 3.11*b* shows the beam on the same screen, once the focus has been moved 2 m downstream the entrance of the plasma. Especially in the horizontal plane, the beam intensity distribution is no longer described by a Gaussian. We also note the asymmetric beam distribution.

Since the uncertainty of the measurement comes from the asymmetry between the two sides of the distribution, I further studied the beam shapes, integrating the projection points along both directions and considering the slope differences. Figure 3.12*a* shows the integrals of the horizontal projection distribution of Figure 3.11*a* integrating from left to right (blue line) and from right to left (orange, reversed for simplicity). The two curves are close and substantially differ from each other only in the range $(-1, 1)$ mm. Figure 3.12*b*, on the other hand, shows the integrals of the horizontal projection distribution of Figure 3.11*b*: the two lines are separated for the whole range due to the asymmetry of the beam intensity distribution. I thus expect the uncertainty on the transverse beam size measurements to increase focusing the beam downstream the measurement location, i.e. the entrance aperture.

The same kind of study has been conducted on the proton beam. Figure 3.13 shows the beam charge distribution of the proton bunch as observed combining the image of scintillating screens (*Imaging Stations*) positioned 2 and 10 meters downstream the exit of the vapor source, when no plasma was present. The light emitted by the screens is split in order to observe independently the inner and outer parts of the proton bunch. In the plot, the two sections of experimental data are interpolated (dotted line).

The core of the distribution can be considered in good approximation parabolic (in logarithmic scale), thus the proton bunch has a transverse Gaussian profile.

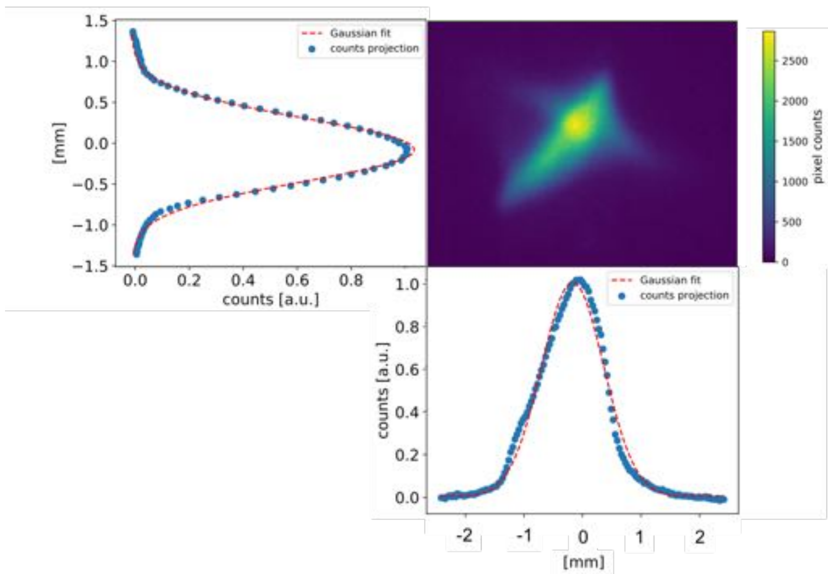

(a)

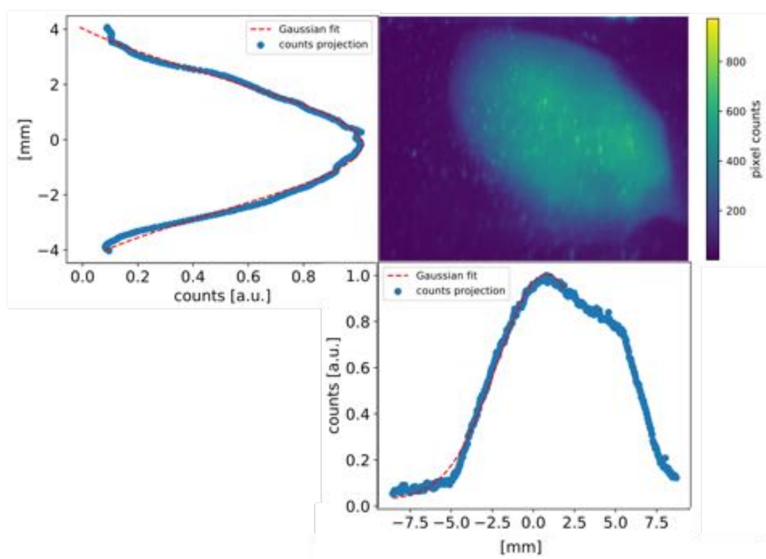

(b)

Figure 3.11: Image of the electron beam on a scintillating screen 0.8 m upstream the plasma entrance. Blue dots are the intensity projections. Dashed red lines indicate Gaussian fits. In (a) the beam is focused on the screen; in (b) it is focused 2 meters downstream the plasma entrance. Horizontal projection in (b) is fitted only for the left-hand side because of a damage on the screen at the bottom right corner.

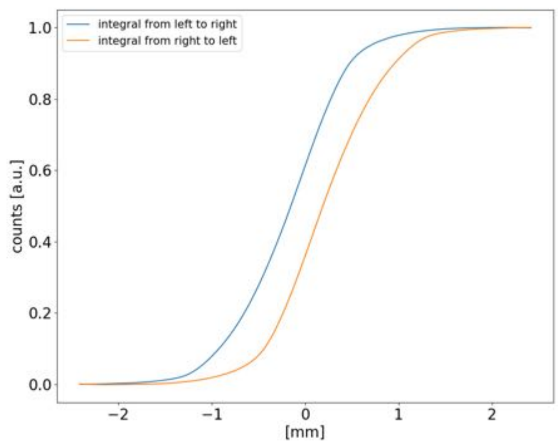

(a)

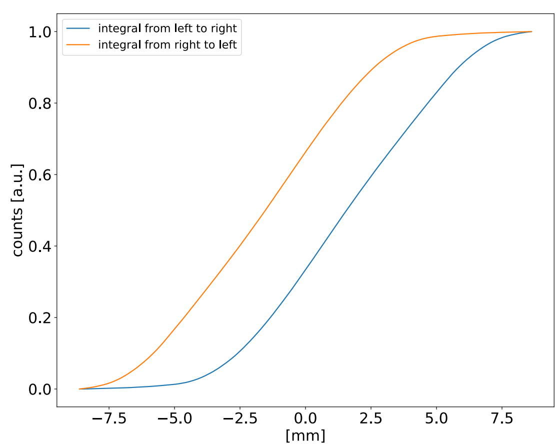

(b)

Figure 3.12: Integrals of the horizontal projection distributions of Figure 3.11a (a) and Figure 3.11b (b). Blue lines are the integrals from left to right, orange lines are the integrals from right to left (reversed for simplicity).

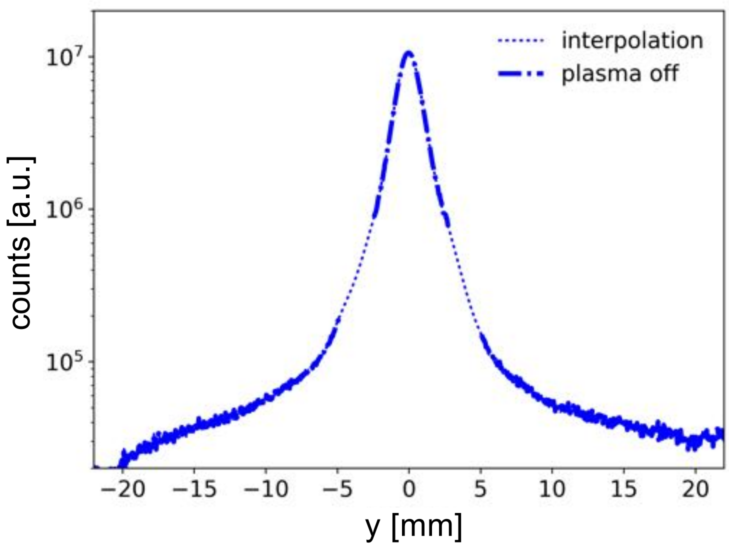

Figure 3.13: Transverse proton beam distribution observed on the Imaging Stations [32] (without plasma). Blue markers are the experimental data, obtained independently for the core and the tails of the distribution. Dotted line is the interpolation between the two datasets.

3.4 The effect of the earth magnetic field on the electron bunch

As explained in Section 2.5.2, we are interested in quantifying the effect of the earth magnetic field on the electron beam trajectory. Since no beam size or position instrument can be installed at the plasma entrance, it is not possible to directly measure the electron beam trajectory deflection. Thus, we developed an indirect measurement technique that uses the BLMs and the vapor source entrance aperture as follows:

1. We establish a position reference on the aperture. Using the proton beam and the proton beam loss monitors we scan (horizontally and vertically) the proton beam position over the entrance aperture (Figure 3.14 shows the horizontal one). We take a position reference on the last two screens upstream the vapor source after aligning the beam at the center of the entrance aperture on both transverse planes. The effect of the earth magnetic field on the 400 GeV/c proton bunch is negligible, so the linear prediction of the proton trajectory is justified (we note that the losses distribution is centered around '0' and centers of the ramps are positioned at $\pm 5\,\mathrm{mm}$).

2. I align the electron bunch onto the proton reference from step 1 using the last two scintillating screens upstream the plasma entrance. I then scan horizontally and vertically the electron beam position over the aperture while recording the BLMs loss signals. Then, I compute the beam position at the iris using the linear prediction (Equation 3.2).

3. If the measured loss distributions (protons and electrons) are not overlapped in space, I manually shift the electron scan to match the proton one; therefore, we determinate the deflection Δs as the distance between the two reference positions: this corresponds to the effect of the earth magnetic field on the electron bunch trajectory. Final values and errors are calculated repeating the manual alignment matching the minimum plateau and the centers of the rise ramps.

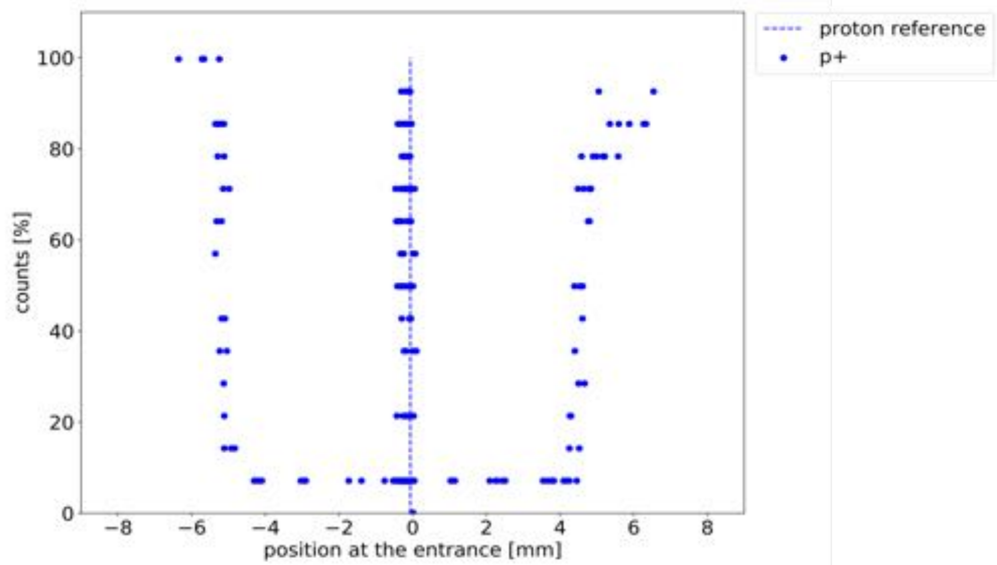

Figure 3.14: Proton horizontal scan of the entrance aperture. Loss signals come from a proton beam loss monitor positioned downstream the entrance and are normalized to 100 %. High loss points around the '0' position are a result of the scan in the vertical direction. The vertical dashed line indicates the reference trajectory at the center of the aperture. The error on the single measurement is ±1 count.

3.5 Electron beam propagation along the vapor source

As already mentioned, it was technically not possible to install any beam position or size diagnostics inside the existing vapor source. Thus, to study the propagation of the electron beam along the source, I used the electron beam loss monitors.

The BLM signals yield an estimation of where along the source losses occur and until where the beam propagates. A small loss signal can mean:

1. no losses occur at the given location;
2. the beam doesn't reach that point.

High losses mean that the electrons are lost close to the detector position.

3.5.1 Propagation in vacuum

We record loss signals while varying the focal point along the vapor source and steering the beam to cross the entrance aperture at its center (parallel propagation, see Figure 3.15).

To visualize the process, I calculated and plotted the electron beam transverse envelope of a $\epsilon_{\mathrm{N}} = 10\,\mathrm{mm{\cdot}mrad}$ beam propagating along the source (Figure 3.15). When the beam is focused at the entrance (Figure 3.15a), the 3-σ envelope passes through the entrance. The beam size evolves according to beam optics: I expect to detect losses further downstream, but not at the entrance. When the focal point is set further downstream, only the charge within the 1-σ envelope passes, while the rest of the beam is stopped at the iris: only a fraction of the beam propagates along the source, and losses take place at the entrance. (Note that calculations don't include the beam dispersion, which increases the transverse beam size outside of the focal point.)

3.5.2 Propagation in plasma

Additionally, I wanted to study electron beam propagation, in presence of plasma. To do this, the beam is focused at the entrance aperture and steered in one of the injection configuration (see Figure 3.16). The laser pulse energy is then varied, while recording the BLM signals. Observation of loss signal on the detector positioned further downstream (at least 6 meters downstream the

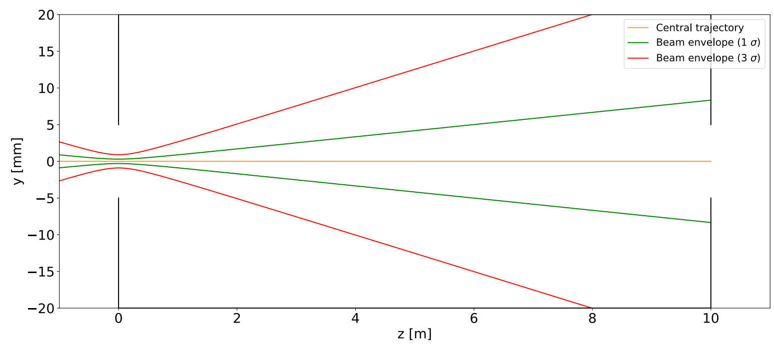

(a)

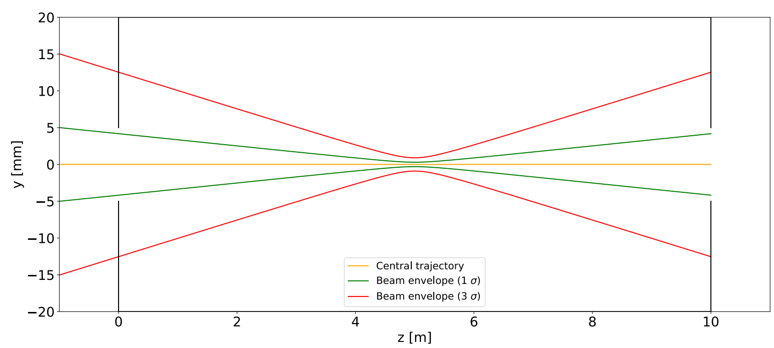

(b)

Figure 3.15: Theoretical electron beam envelope for a normalized emittance of 10 mm·mrad along the vapor source. In orange the central trajectory, in green 1-σ envelope, in red 3-σ envelope. Black lines at 0 and 10 m show the entrance and exit apertures. Calculations are for focus at the entrance (a) and 5 m downstream (b).

entrance aperture) would confirm the guiding of electrons through the plasma channel [46].

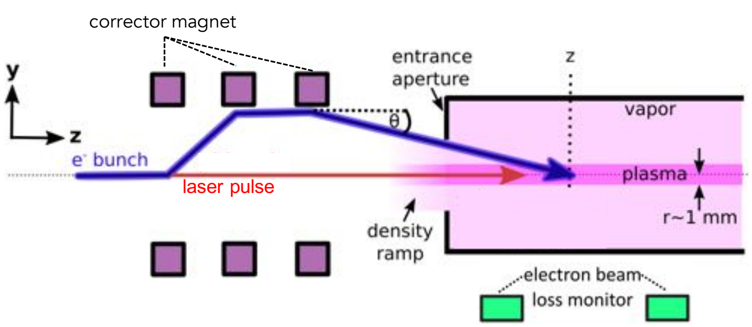

Figure 3.16: Schematic of the oblique injection of the electron beam into the plasma [25]. The electron beam (blue arrow) receives a vertical offset and a downward kick by the last three corrector magnets. This way, electrons avoid the plasma electron density ramp and are injected into the plasma channel at a defined location z downstream the entrance.

3.6 Detection of beam losses during the injection experiment

The main goal of the BLM system during acceleration experiment is to observe electron beam losses during the injection. For example, the electron bunch particles can miss the proton-driven wakefield, continuing on their straight trajectory; or they can interact with the defocusing fields of the plasma-wave and thus be reflected, as mentioned in Section 2.1.3 and illustrated by LCODE simulations shown in Figure 3.17. In this simulation, a part of the injected electrons is captured by the wakefield and accelerated along the plasma. The rest of the electrons are not captured. They exit the plasma and interact with the material of the vapor source. Given enough energy deposit in the BLM, we can detect the location of the losses along the plasma.

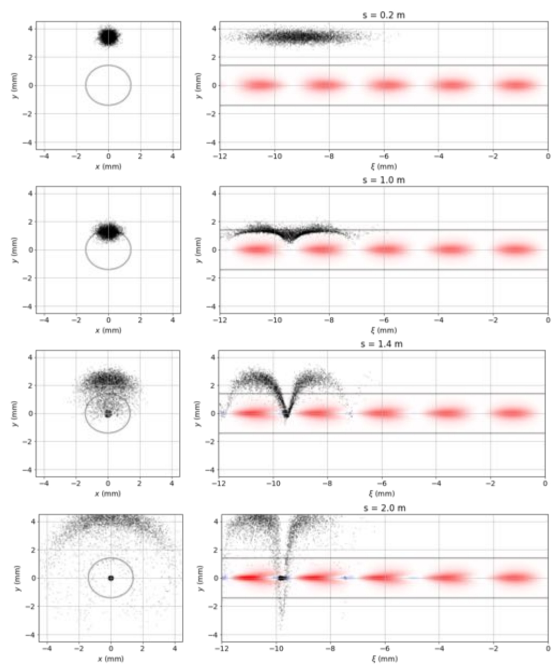

Figure 3.17: LCODE simulation results of the injection of electrons (black) into the wakefields driven by self-modulated proton bunch (red) at different positions along the plasma (s) in the proton bunch rest frame. On the left-hand side, transverse view of the beam particle distribution; on the right-hand side, longitudinal view along the proton bunch and plasma.

To perform this measurement, we need to detect the electron loss on top of the background produced by the protons. To do this, we processed the events in presence of protons as explained in Section 3.2.

If electrons are injected into the wakefields, I expect to detect an increase of the electron loss signals for detectors positioned downstream of the injection point.

3.7 Conclusions

In this Chapter, I illustrate the beam loss monitor setup and the working principle of the detectors.

I also discuss the major background sources for measurements with only the electron beam as well as when the proton beam is present.

I present and discuss the measurement techniques for measuring the electron transverse beam size at the plasma entrance, the trajectory deflection caused by the earth magnetic field, the propagation along the vapor source, and beam losses during the acceleration experiment.

Chapter 4

Experimental results

I use the electron beam loss monitor setup described in Section 3.1 to measure properties of the AWAKE electron beam. I study beam propagation along the vapor source and losses due to injection in proton-driven wakefields.

The measurements discussed were performed during the AWAKE measurement campaigns in May, July, September and November 2018. During these periods, most of the efforts were dedicated to studies on electron acceleration (observed for the first time in May 2018 [16]) and to improve the performance of the accelerator.

4.1 Transverse beam size measurements

4.1.1 Validation of the measurement technique

To validate the technique described in Section 3.3, I first performed the measurement with the proton pilot beam (bunch population of $1{\cdot}10^{11}$ particles per bunch) delivered by the SPS. This beam is well characterized and its r.m.s. bunch size at the plasma entrance well known: (0.10 ± 0.01) mm, scaled from the beam size measured with foils emitting Optical Transition Radiation and the beam emittance measured in the SPS machine. Moreover, the bunch core has a Gaussian transverse beam charge distribution, as discusses in Section 3.3.1 and shown in Figure 3.13.

We performed a vertical scan of the entrance aperture with the proton beam, measuring losses with the electron beam loss monitors (shown in Figure 4.1). The determined transverse r.m.s. beam size $\sigma = (0.11 \pm 0.02)$ mm is compatible with its predicted value.

This means that the measurement technique described in Section 3.3 is valid and can thus be used to measure the transverse beam size of the electron beam at the entrance aperture.

I observe that the minimum of losses in the proton scan is $\sim 50\,\%$ of the maximum, because of the high-level background generated by the proton bunch even when it is centered on the beam line, as discussed in Section 3.2.

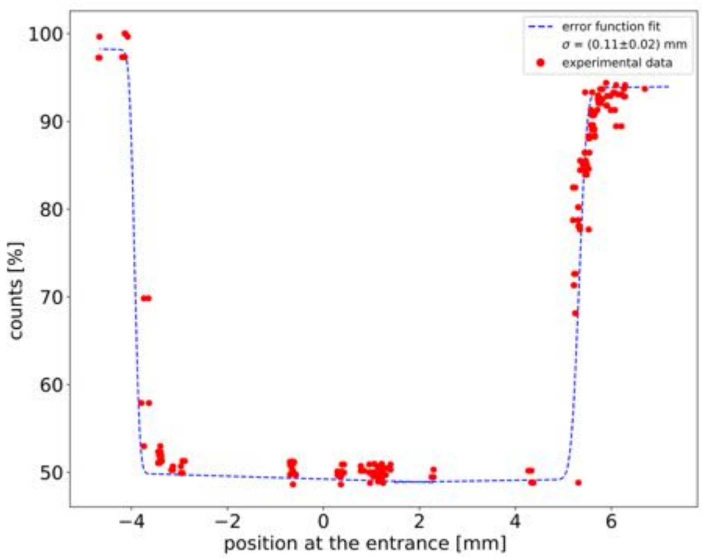

Figure 4.1: Proton beam vertical scan of the entrance aperture. Every point is the result of a single measurement; errorbars, not visible over the markers, are the intrinsic measurement uncertainties (± 0.22). Each loss ramp is fitted with an error function. Final σ is the mean of the two results.

4.1.2 The transverse electron beam size measurements

I measured the amount of losses as a function of the electron beam position at the plasma entrance as described in Section 3.3 for different focal point positions (-0.8, 0, 1, 2, 4 m) with respect to the entrance aperture, and for two beam charges (200 and 600 pC).

Figure 4.2 shows the results for the horizontal (4.2*a*) and vertical (4.2*b*) planes for an electron bunch with a charge of 200 pC and focused at the entrance aperture. We note that the minimum of the losses is around $5\,\%$ and thus close to zero: this means that, when the beam is centered on the aperture, very few particles interact with the material. As soon as a significant amount of beam particles hit the aluminum foil, losses increase, reaching a maximum when all beam particles interact with the iris. The beam size was measured to be $\sigma_{\mathrm{x}} = (0.45 \pm 0.02)\,\mathrm{mm}$ and $\sigma_{\mathrm{y}} = (0.33 \pm 0.04)\,\mathrm{mm}$.

Figure 4.3 shows the scans for the beam focused 2 m downstream. In this configuration, the minimum losses are higher than when the bunch is focused at the plasma entrance and transitions between minimum and maximum loss are longer. Both effects are due to the increase of the beam size at the measurement location: the transverse beam size at the plasma iris increases as the bunch is focused further downstream, as expected and discussed in Section 2.5. The beam size at the plasma entrance was in fact measured to be: $\sigma_{\mathrm{x}} = (2.22 \pm 0.03)\,\mathrm{mm}$ and $\sigma_{\mathrm{y}} = (0.62 \pm 0.02)\,\mathrm{mm}$.

Table 4.1 summarizes the measured transverse beam size for different focus positions and bunch charges:

bunch charge	beam size	focal point [m]				
		-0.8	0	1	2	4
200 pC	σ_{x} [mm]	1.1±0.2	0.45±0.02	1.2±0.2	2.22±0.03	2.6±0.4
	σ_{y} [mm]	0.38±0.05	0.33±0.04	0.5±0.1	0.62±0.02	0.9±0.1
600 pC	σ_{x} [mm]	1.02±0.01	0.53±0.02	1.8±0.4	3±1	3±1
	σ_{y} [mm]	0.5±0.1	0.49±0.05	1.13±0.03	1.42±0.08	2.0±0.4

Table 4.1: Transverse beam size obtained from error function fit of the entrance aperture scan for different optics and beam charges. Values are the average of the two ramps, errors the standard errors.

For both beam populations, when the beam is focused at the entrance aperture (i.e. at the measurement location), it is transversely round and it has its minimum size. This agrees with the theoretical beam optics (Section 2.5) [42]: moving the beam focus at different locations increases both transverse sizes at the entrance. We note that the measured σ values for beam focused at the entrance are in good agreement with theoretical ones: $\sigma_{200,\mathrm{th}} \sim 0.23\,\mathrm{mm}$ and $\sigma_{600,\mathrm{th}} \sim 0.32\,\mathrm{mm}$ (calculated not including the beam dispersion). In fact, all along the electron beamline we measure transverse beam sizes (using BTVs) slightly larger than expected from theory. The horizontal beam size grows more than the vertical one because of the optics of the transfer beam line and the notfully compensated dispersion. Therefore, focusing the beam downstream makes it bigger at the entrance, causing losses before the beam enters the plasma.

Measured beam sizes increase with the bunch charge for all focal point positions. The ratio between sizes is shown in Figure 4.4: at the focal point, $\sigma_{600} = (1.48 \pm 0.05)\sigma_{200}$, as expected from the discussion in Section 2.5. Moreover, the ratio increases up to 2.3±0.3 moving the focal point further downstream.

Uncertainties on the measurements increase moving the focal point downstream the measurement location. In fact, as discussed in Section 3.3.1, when the beam size becomes larger, its transverse profile significantly deviates from a Gaussian one (as shown in Figure 3.11) and is asymmetric due to imperfections in beam production and transport. Apart from that, a larger σ complicates the fit as the electron beam (or its tails) might interact with both sides of the entrance aperture simultaneously. Figure 4.5 shows the most asymmetric measurement. The asymmetry is evident, as well as the lack of a minimum plateau: the total beam size in this configuration ($\sigma_{\mathrm{x}} = (3.0 \pm 1.0)\,\mathrm{mm}$) is comparable to the entrance aperture radius; hence, as soon as one side completely enters the plasma, the other one starts interacting with material and inducing the loss signal.

4.1.3 Conclusions

Scanning the electron beam across the entrance aperture while recording the BLM loss signals allows me to determine the transverse size of the beam at the plasma entrance. I note that the results are reliable if the transverse bunch size is much smaller than the opening aperture. Because of the complex design of the rubidium vapor source, no other diagnostics can be positioned at this location, hence this measurement gives the most downstream information on the beam before it enters the plasma. For the 200 pC electron bunch, the transverse beam size (σ_{x}, σ_{y}) at the entrance increases from $(0.45 \pm 0.02,\ 0.33 \pm 0.04)\,\mathrm{mm}$ to $(2.6 \pm 0.4,\ 0.9 \pm 0.1)\,\mathrm{mm}$ as the beam is focused further inside the plasma. Furthermore, I observed the beam size to increase with the charge as $\sigma_{600} \sim \sqrt{2}\sigma_{200}$, as expected from theoretical predictions.

To maximize the charge transported into the source, we focus the beam as close as possible to its entrance. On the other hand, to increase the probability of injecting most of the beam at the right phase of the wakefields, we would like to minimize the spot size of the electron beam at the crossing location. As a result of these measurements, a trade-off had to be found, in order to increase the efficiency of the charge capture and of the acceleration process: the beam focal point and injection were set at one meter inside the plasma. The beam size at the entrance is then: $\sigma_{\mathrm{x}} = (1.2 \pm 0.2)\,\mathrm{mm}$ and $\sigma_{\mathrm{y}} = (0.5 \pm 0.1)\,\mathrm{mm}$. In this configuration, beam losses at the entrance are still acceptable while the spot size at the injection is minimized, even in the oblique electron injection configuration.

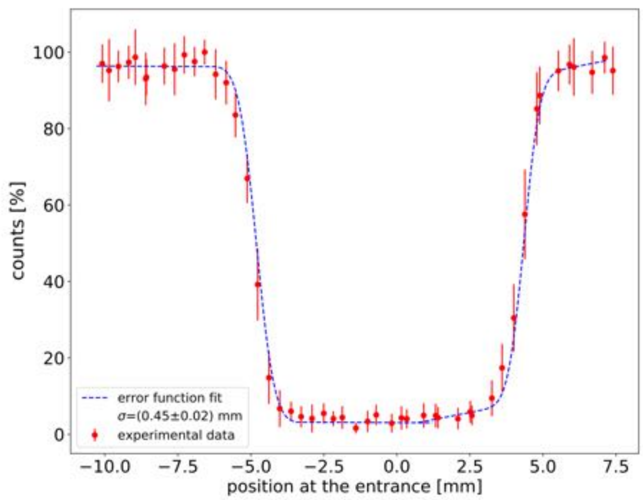

(a) Horizontal scan

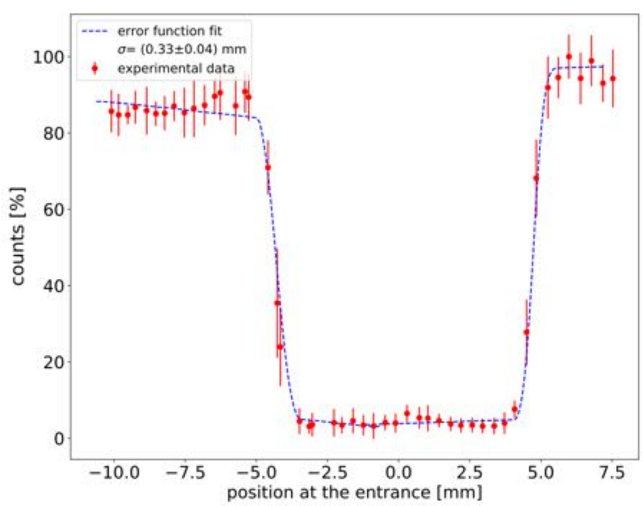

(b) Vertical scan

Figure 4.2: Measured loss signals (red dots) as a function of the linearly reconstructed horizontal (a) and vertical (b) position of the electron beam at the plasma entrance. The '0' position marks the theoretical center of the aperture. Every point is the mean value of 20 measurements; errorbars are the standard errors. Each side of the plot is fitted with an error function (blue dashed lines). The resulting σ as well as its error is given in the Figure legend. For these measurements the 200 pC electron beam was focused at the plasma entrance (measurement location). Fit limits were chosen manually, to optimize the agreement between fit and data.

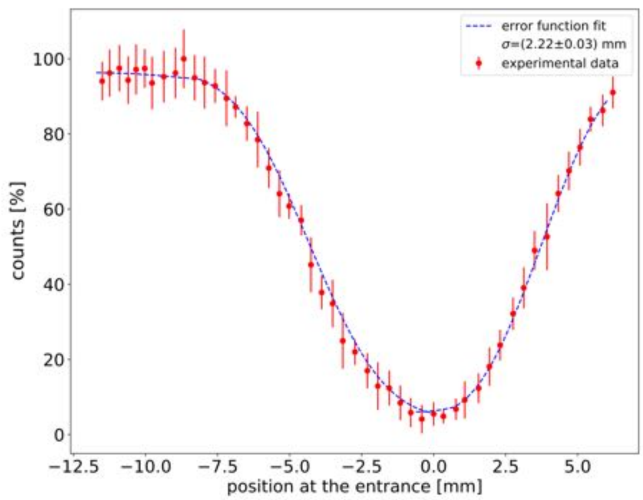

(a) Horizontal scan

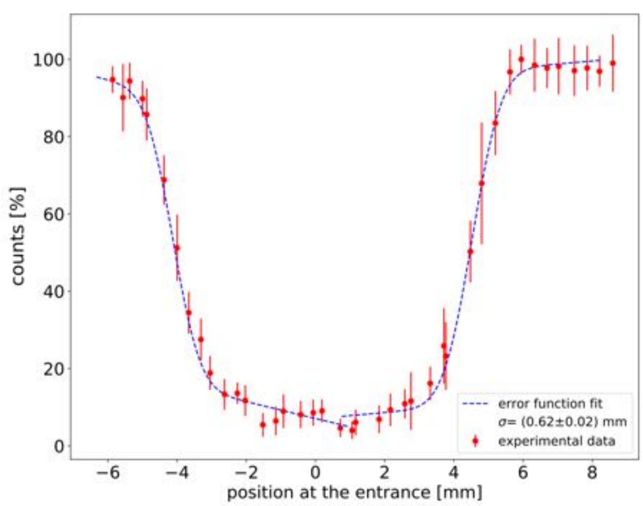

(b) Vertical scan

Figure 4.3: Measured loss signals (red dots) as a function of the linearly reconstructed horizontal (a) and vertical (b) position of the electron beam at the plasma entrance. The '0' position marks the theoretical center of the aperture. Every point is the mean value of 20 measurements; errorbars are the standard errors. Each side of the plot is fitted with an error function (blue dashed lines). The resulting σ as well as its error is given in the Figure legend. For these measurements the 200 pC electron beam was focused 2 meters downstream the entrance aperture. Fit limits were chosen manually, to optimize the agreement between fit and data.

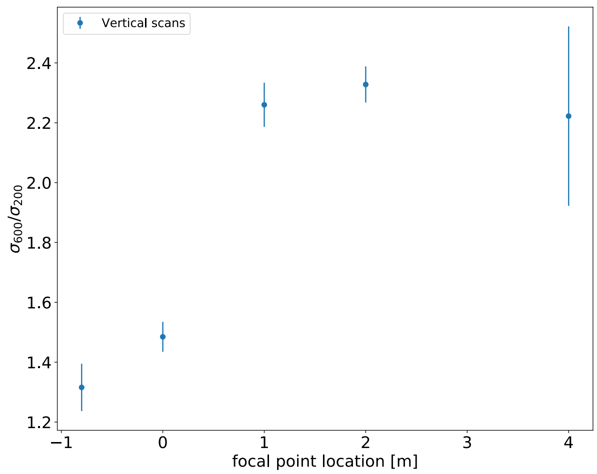

Figure 4.4: Ratio of vertical size of the two electron beams with different amount of total charge. σ_{600} and σ_{200} are the r.m.s. beam sizes of the 600 pC and 200 pC beams respectively.

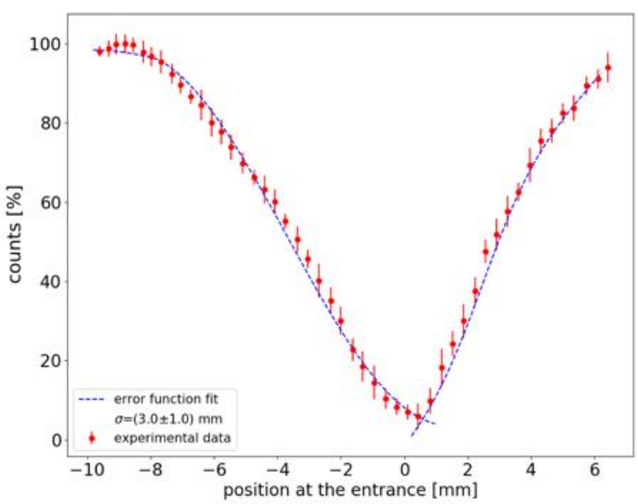

Figure 4.5: Horizontal scan, focusing the 600 pC beam 2 m downstream the entrance.

4.2 The effect of the earth magnetic field on the electron bunch

Following the procedure illustrated in Section 3.4, we aligned the electron bunch onto the proton reference trajectory using the last two scintillating screens upstream the plasma entrance. We then run the horizontal and vertical scans of the aperture recording the BLMs loss signals and computing the beam position at the iris using the linear prediction (Equation 3.2).

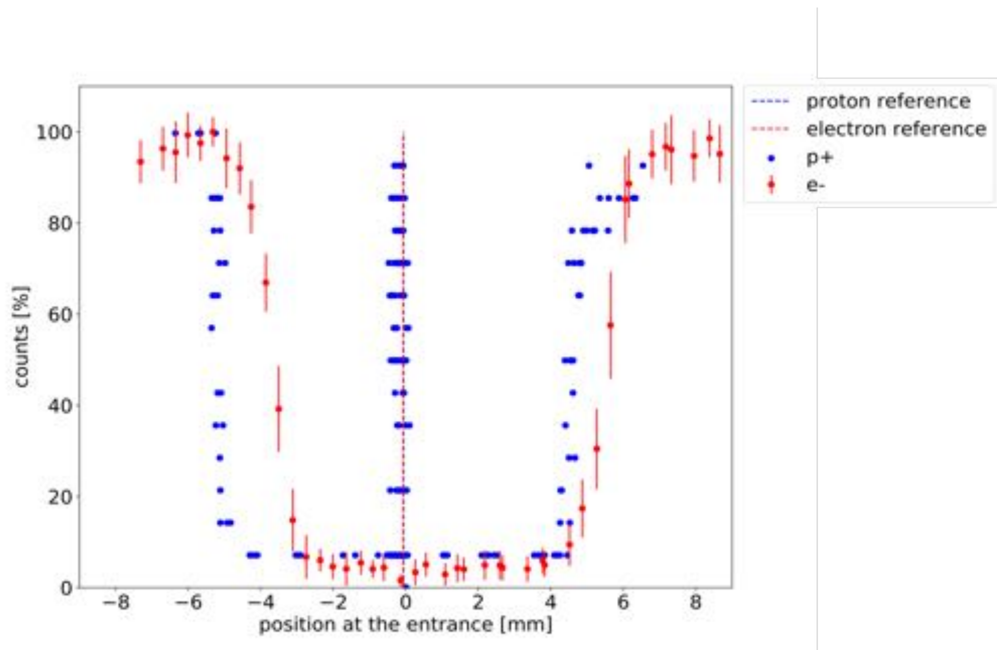

Figure 4.6: Electron (red dots) and proton (blue dots) horizontal scans, aligning reference trajectories (red and blue dashed lines). The position at the entrance is computed linearly for both beams.

As clearly visible on Figure 4.6, loss distributions of the proton and electron scans are not overlapped in space: the electron scan is shifted by a constant amount with respect to the proton one. Manually overlapping the two scans, I aligned the electron beam losses distribution on the entrance iris (Figure 4.7).

Calculating the discrepancy Δs between the two reference trajectories gives an estimate of the effect of the angular deflection caused by external fields, e.g. the earth field.

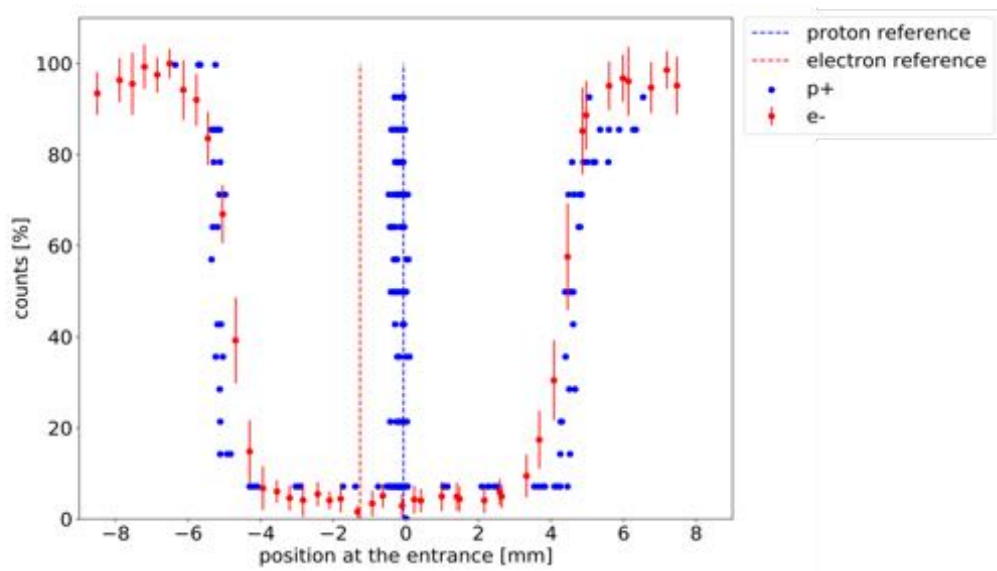

Figure 4.7: Electron (blue dots) and proton (red dots) horizontal scans, shifting shapes such that centers of ramps overlap. Discrepancy between reference trajectories (red and blue dashed lines) gives the value of the deflection caused by the earth magnetic field on the electron beam.

The measured values are:

- Horizontal plane: (-1.2 ± 0.1) mm (bending to the right);
- Vertical plane: (-0.4 ± 0.1) mm (bending downward).

We note the excellent agreement (in both direction and amplitude) with the theoretical calculations discussed in Section 2.5.2 (Horizontal: 1.33 mm to the right; vertical: 0.66 mm downward).

Since the measured values are compatible with the predicted angle deflections, we can state that the earth magnetic field bends the electron bunch trajectory. Consequently, we compensated this deflection with the last corrector magnets. This allowed us to reach true electron-proton beam alignment at the plasma entrance. This trajectory was then used as a reference for injection. Indeed, Figure 4.8 shows the final alignment of the beams at the plasma entrance: the electron beam trajectory is predicted using upstream BPMs measurements.

It shows that proton and electron beams overlap at the plasma entrance, after compensation of the earth magnetic field effect.

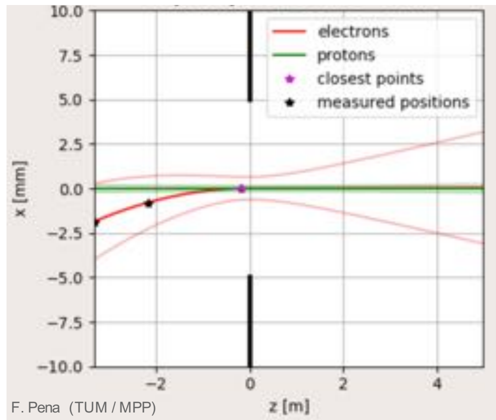

Figure 4.8: Prediction of beam trajectory alignment. The calculations include the effect of the earth magnetic field. The green line shows the trajectory of the proton bunch. The red lines show the central trajectory as well as the 1-σ transverse beam envelope of the electron bunch. Black vertical lines indicate the location of the aperture of the entrance iris. Black stars show the beam positions as measured by the BPMs; the calculated position where trajectories are at their closest point is indicated by the purple star.

4.3 Studies of electron beam propagation along the vapor source

As explained in Section 3.5 we recorded loss signals while varying the focal point along the vapor source (from 2 m upstream to 6 m downstream, in one-meter steps). The 600 pC beam was steered to cross the entrance aperture at its center and to propagate on-axis. The resulting loss signal distribution for two detectors, positioned 1.5 m and 6.0 m downstream the entrance, is shown in Figure 4.9.

As expected, losses observed at the entrance are minimum when the focus is positioned at the entrance, as the transverse bunch size is minimum. Very few particles interact with the material of the entrance layer. As illustrated in Figure 3.15 and measured in Section 4.1, moving the focal point downstream

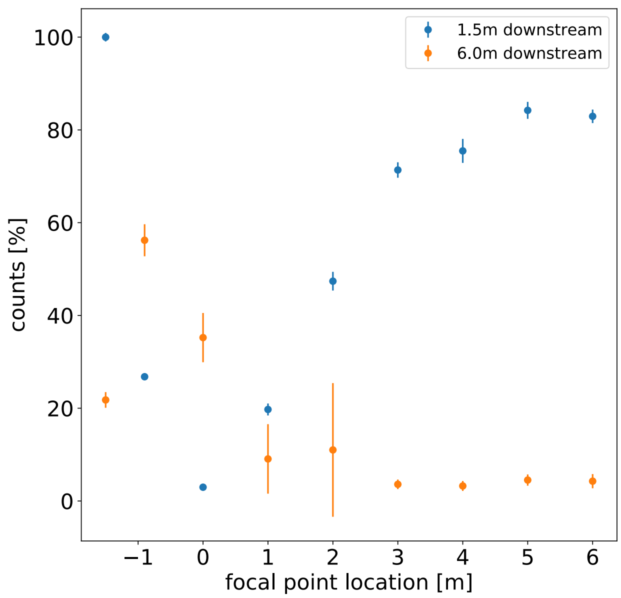

Figure 4.9: Loss signals as a function of the focal point position for the 600 pC beam centered on the entrance aperture. Blue markers refer to the BLM positioned 1.5 m downstream the entrance; orange markers refer to the BLM positioned 6.0 m downstream the entrance. Both detectors are placed below the vapor source. Data points are the mean value of 10 measurements and normalized to 100 % over the maximum of the dataset; errorbars are the standard errors.

makes the beam size bigger at the entrance, causing losses, indeed recorded by the close detector. The detector positioned further downstream (6 m, below the vapor source) shows the inverse trend. Losses have their maximum when the beam completely passes the entrance, and they drop when it is clipped on the entrance iris. As mentioned above, in this case small signal can also mean that few particles reach the detector location rather than an efficient transmission of the beam. In fact, when the beam is focused at the entrance, most of the beam passes the entrance and evolves according to beam optics: losses are detected further downstream, but not at the entrance. When the focal point is set further downstream, only the charge within 1-σ envelope passes, while the rest of the beam is stopped at the iris (see Figure 3.15): I observe high losses at the entrance and that only a fraction of the beam propagates along the source.

I additionally measured electron beam propagation, in presence of plasma (Rb density was set to $2.05 \cdot 10^{14}\,\mathrm{cm}^{-3}$). The 600 pC electron beam was focused at the entrance aperture and steered in the oblique injection configuration as explained in Section 3.5.2. The laser pulse energy was increased from 0 to 60 mJ, in 9 unequal steps. Figure 4.10 shows loss signals of detectors positioned 1.5 and 6 m downstream the entrance as a function of the laser pulse energy. Varying the energy of the laser pulse changes the total number of ionized Rb atoms and, according to laser propagation studies [17], the plasma radius increases.

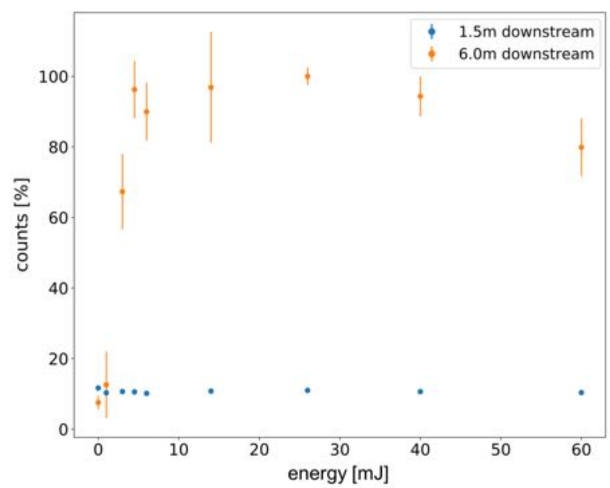

Figure 4.10: BLM loss signals as a function of laser pulse energy. Data points show the mean value of 10 measurements normalized over the maximum of the dataset; errorbars are the standard errors. Blue markers show measurements of the detector 1.5 m downstream the entrance; orange markers show the readings from the detector 6 m downstream. Rb density was set to $2.05 \cdot 10^{14}\,\mathrm{cm}^{-3}$.

The detector positioned close to the entrance shows no dependencies with the laser pulse energy: this could mean that electrons are actually injected into the plasma further downstream, and they are not affected by the presence of plasma at the entrance. The detector at 6 meters downstream shows a different trend. No losses are detected when there is no laser or its pulse energy is < 2 mJ: as mentioned above, this could mean that the beam doesn't reach the detector location; losses sharply increase with the laser pulse energy: this could be due to guiding of electrons in the plasma channel. The hypothesis that electrons are guided by the plasma channel is confirmed by the observation of electrons on the spectrometer scintillating screen (Figure 4.11).

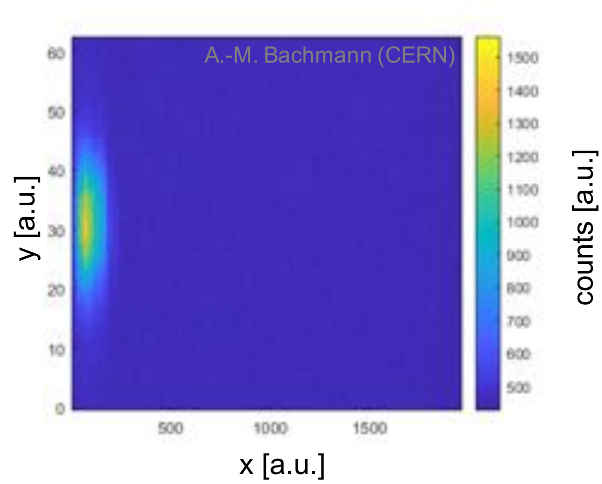

Figure 4.11: Electron beam on the spectrometer scintillating screen. The beam energy is dispersed by a dipole magnetic field and thus energy resolved.

This measurement showed that, using the vertical oblique injection scheme, it is possible to inject part of the electron beam into the plasma channel generated by the laser pulse. It also proves correct electron-laser pulse alignment. This trajectory was then used as a reference during the acceleration experiment.

4.4 Detection of beam losses during the injection experiment

Even with the background subtraction, it was still challenging to observe a clear signal from the electrons on the electron beam loss monitors, in presence of the proton beam. Thus, we collected a dataset while acceleration was consistently observed. The plasma electron density was $2 \cdot 10^{14}\,\mathrm{cm}^{-3}$ and the electron bunch charge $\sim 550\,\mathrm{pC}$. The 124 events are divided in three categories:

1. electrons and plasma;
2. protons and no plasma;

3. protons, electrons and plasma.

Signals are processed and background subtracted as explained in Section 3.1 and 3.2. The data are then averaged. Categories 2 and 3 are shifted for zeroing the "protons and no plasma" category: in fact, we are interested on the discrepancy between values rather than on their absolute values.

Figure 4.12*a* shows the results: after background subtraction loss signals are higher if electrons are present, for all detectors. This shows that the BLM system is sensitive to electron losses in presence of protons. Moreover, detectors positioned further than 6 meters downstream the plasma entrance give signals higher than only electron ones.

This is a clear evidence that electron losses are higher in the presence of plasma wakefields. The extra signal could be a result of electrons reflected by the wakefields and/or electrons dephased into the defocusing fields of the wave, being expelled out of the plasma. We repeated the measurement for different setups, and no dependencies of losses with respect to injection parameters (e.g. alignment or relative delay between beams) have been observed. This may be explained considering that a few percentage (less than 2 %) of the beam is actually accelerated and transported till the end of the plasma source and that defocused electrons are spread out with very large angle, losing their initial direction.

In conclusion, the electron beam loss monitors are sensitive to electron loss signals even in presence of the protons. Background reduction and subtraction increased the signal to noise ratio and enabled the detection of defocused electrons during the injection process. Defocusing process may occur because of reflection of particles when they enter the plasma or because of dephasing in the defocusing part of the wakefields.

4.5 Satellite pre-bunches detection

As explained in previous Sections, background estimation, reduction and subtraction were crucial issues to be solved, in order to correctly conduct measurements on electron losses in presence of the proton beam. Studying the analogue signals generated by the detectors in presence of protons, we observed loss signals in front of the main proton peak (which is synchronized with the electron beam). These "pre"-signals couldn't be related to electronics, since they were synchronized between all detectors, that are slightly different from each

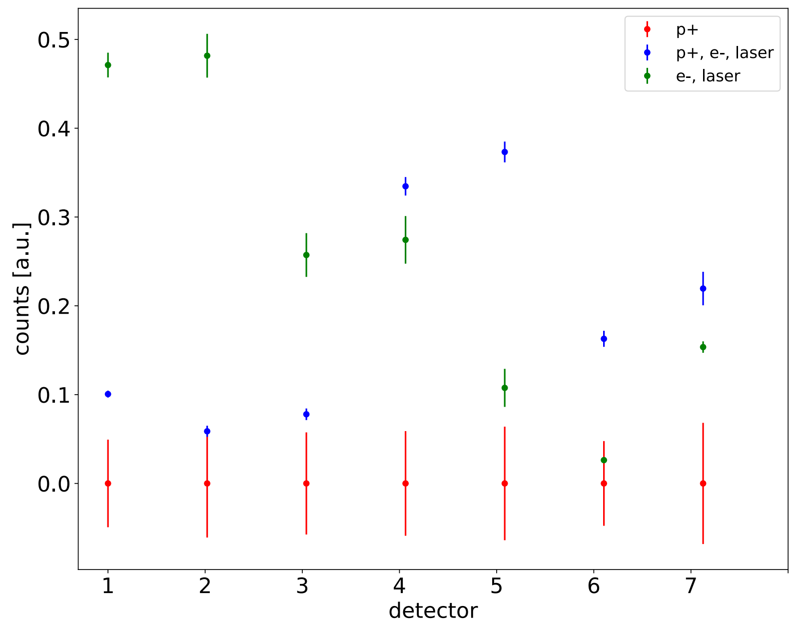

(a) Measured loss signal amplitude during the experiment for different detectors. Data are averaged values of 124-event data sample, divided by categories; errorbars show the standard errors. Detector numbers refer to Figure (b).

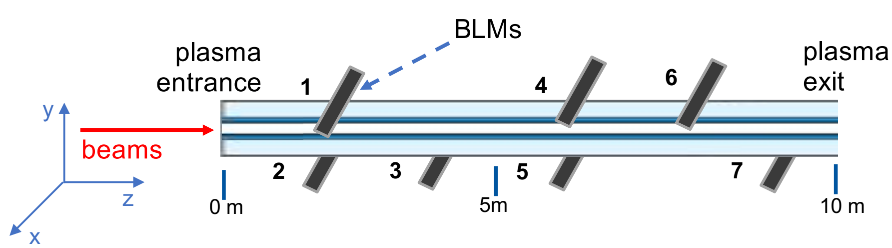

(b) Electron beam loss monitor setup along the vapor source.

Figure 4.12

other; they couldn't be generated by secondary particles, because they would have needed to be faster than the primary proton beam (proton beam $\gamma = 427$, $\beta = 0.99997$); and they couldn't indicate a saturation effect of the detectors, because they would have appeared after the main proton beam signal.

As shown in Figure 4.13, streak camera images confirmed that these peaks were real and generated by low-populated proton bunches delivered by the SPS, up to ~ 285 ns in front of the main bunch. Moreover, both timing and charge of the pre-bunches agree between the two diagnostics.

Pre-bunches are formed during the bunch rotation process in the SPS machine [47]; after proving their existance, their number and population were decreased by reducing the step voltage during the bunch-rotation process.

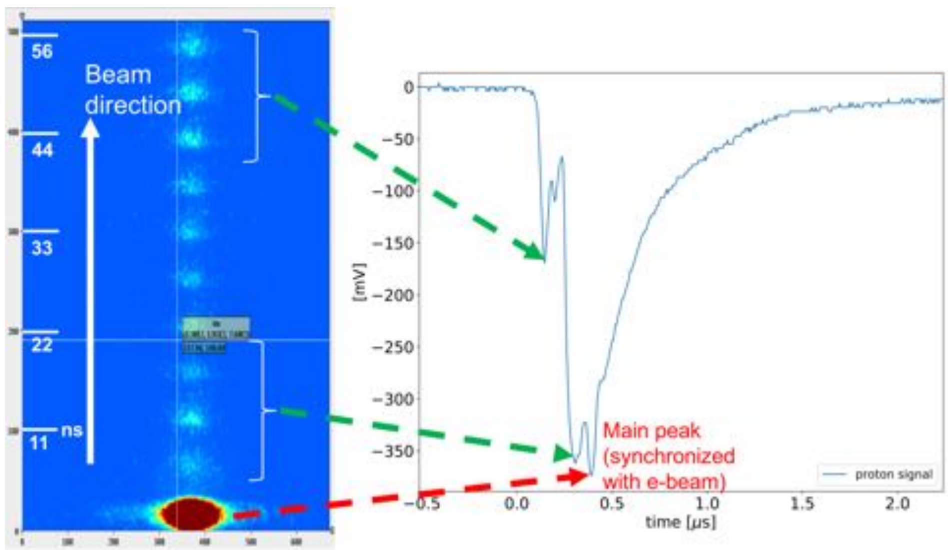

Figure 4.13: Streak camera image of the proton pre-bunches, correlated with beam loss monitor analogue signal.

4.6 Conclusions

Using the electron beam loss monitor setup, I conducted measurements on the AWAKE electron beam.

Studying losses at the entrance aperture, I measured the transverse beam size of the electron beam for different optics and beam charges. This measurement helped us to understand the beam characteristics and losses before the bunch enters the plasma: in fact, no other diagnostics can be positioned at that location, thus the BLMs provide the most downstream information on the beam before injection.

Using the same technique, I indirectly estimated the electron beam deflection from the straight trajectory caused by the earth magnetic field, contributing to improve our spatial beam alignment tools and thus the injection process.

Detecting losses gives information on the beam propagation along the vapor source. I estimated electron beam losses at the entrance for different beam focusing optics and studied the propagation of electrons in vacuum and within the plasma channel.

I observed an increase of electron beam losses during the acceleration experiment; this may indicate a defocusing effect of plasma wakefields on the injected electron beam.

Studying the background generated by the proton beam, I observed satellite pre-bunches ahead of the main proton bunch. This observation was then confirmed by time-resolved streak camera images.

Chapter 5

Summary & Conclusions

5.1 Conclusions of the work presented in this thesis

In this thesis, I study properties of the electron beam in the AWAKE experiment, using the electron beam loss monitors setup. The following points were addressed:

- The electron transverse beam size at the entrance aperture of the vapor source increases moving the focal point downstream into the plasma, causing charge losses on the entrance iris;
- Using the BLM setup, I was able to prove that the electron beam trajectory is affected by the earth magnetic field. Further, the experimental measurements agree with the theoretical predictions. Quantifying the deflection helped to improve the alignment tool for the injection experiment;
- Electrons injected into the plasma are transported along the source by laser-guiding as the loss signals at the downstream detectors increase in presence of plasma;
- Electron losses downstream the injection point increase during the acceleration experiment: this may be explained considering defocusing wakefields acting on part of the injected electron bunch.

The electron beam loss monitors setup showed to be sensitive enough to conduct measurements on the electron beam only, as well as in presence of the proton bunch. Background reduction turned out to be the most challenging issue to overcome, and limited the performance of the system during the acceleration experiment. However, this detection system has become a crucial tool to optimize the electron injection during the experimental measurements.

The BLM setup could be improved using scintillating fibers. This kind of detectors would be easier to install and would allow to position more detectors along and around the vapor source, possibly increasing the spatial resolution of the system.

5.2 Long term outlook for AWAKE

AWAKE is a R&D proof-of-principle experiment and the final goal is to design and build an electron accelerator at TeV energies.

So far, the experiment was able to demonstrate the development of plasma wakefields driven by a self-modulated proton bunch in the 10 m of plasma, as well as to accelerate externally injected electrons up to $\sim 2\,\mathrm{GeV}$.

The next step for AWAKE is to control the proton bunch, plasma and laser parameters. To create an electron bunch with tens of GeV, a micron-level normalized emittance, a percent level relative energy spread and an electron bunch charge of $0.2 - 1\,\mathrm{nC}$ is the goal of AWAKE Run 2, which is scheduled from 2021 onwards.

If Run 2 were successful a proposal for a proton driven plasma wakefield accelerator producing electrons with $50 - 100\,\mathrm{GeV}$ for fixed target physics would be prepared as an intermediate step before proposing a plasma-based high-energy electron-proton physics collider [12].

Bibliography

[1] T. Tajima et al., "Laser Electron Accelerator," *Physical Review Letters,* ***43***, 1979.

[2] C. E. Clayton et al., "Ultrahigh-Gradient Acceleration of Injected Electrons by Laser-Excited Relativistic Electron Plasma Waves," *Physical Review Letters,* ***70***, 1993.

[3] D. Strickland and G. Mourou, "Compression of Amplified Chirped Optical Pulses," *Optics Communications*, 1985.

[4] P. Chen et al., "Acceleration of Electrons by the Interaction of a Bunched Electron Beam with a Plasma," *Physical Review Letters,* ***54***, 1985.

[5] J. B. Rosenzweig, "Experimental Observation of Plasma Wake-Field Acceleration," *Physical Review Letters,* ***61***, 1988.

[6] I. Blumenfeld et al., "Energy Doubling of 42 GeV Electrons in a Metre-Scale Plasma Wakefield Accelerator," *Nature* ***445****, 741-744*, 2007.

[7] W. Klaus, *The Physics of Accelerators.* Oxford University Press, 2000.

[8] CLIC Conceptual Design Report, A Multi-TeV Collider based on CLIC Technology, Geneva, 2012.

[9] V. Shiltev, "Crystal Ball: On the Future High Energy Colliders," *PoS EPS-HEP2015 515*, 2015.

[10] E. Adli et al., "A Beam Driven Plasma-Wakefield Linear Collider: From Higgs Factory to Multi-TeV," *Proceedings of IPAC*, 2014.

[11] W. Leemans and E. Esarey, "Laser-Driven Plasma-Wave Electron Accelerators," *Physics Today*, 2009.

[12] A. Caldwell et al., "Proton-Driven Plasma-Wakefield Acceleration," *Nature Physics*, 2009.

[13] E. Gschwendtner et al., "AWAKE, The Advanced Proton Driven Plasma Wakefield Acceleration Experiment at CERN," *Nuclear Instruments and Methods in Physics Research A, **829**, 76-82*, 2016.

[14] P. Muggli et al., "AWAKE readiness for the study of the seeded self-modulation of a 400GeV proton bunch," *Plasma Physics and Controlled Fusion, **60**, 014046*, 2018.

[15] A. Caldwell and M. Wing, "VHEeP: a very high energy electron–proton collider," *The European Physical Journal C **76**, 463*, 2016.

[16] E. Adli et al., "Acceleration of electrons in the plasma wakefield of a proton bunch," *Nature*, 2018.

[17] J. T. Moody *, MPP, private communication.*

[18] S. Mazzoni et al., "Beam Instrumentation Developments for the Advanced Proton Driven Plasma Wakefield Acceleration Experiment at CERN," *Proceedings of IPAC*, 2017.

[19] M. Turner et al., "The Two-Screen Measurement Setup to Indirectly Measure Proton Beam Self-Modulation in AWAKE," *Nuclear Instruments and Methods in Physics Research A, **829** 3-16*, 2017.

[20] K. Rieger et al., "GHz Modulation Detection using a Streak Camera: Suitability of Streak Cameras in the AWAKE Experiment," *Review of Scientific Instruments, **88**, 025110*, 2017.

[21] F. Keeble et al., "The AWAKE Electron Spectrometer," *Proceedings of IPAC*, 2018.

[22] A. Caldwell et al., "Path to AWAKE: Evolution of the concept," *Nuclear Instruments and Methods in Physics Research A, **829** 3-16*, 2016.

[23] G. Pluyshchev et al., "A Rubidium vapor source for a plasma source for AWAKE," *Journal of Physics D: Applied Physics*, 2017.

[24] K. V. Lotov et al., "Electron trapping and acceleration by the plasma wakefield of a self-modulation proton beam," *Physics of Plasmas **21**, 123116*, 2014.

[25] M. Turner et al., "External electron injection for the AWAKE experiment," *Proceedings of AAC*, 2018.

[26] R. Fitzpatrick, *Introduction to Plasma Physics: a graduate level course.*

[27] E. Esarey et al., "Overview of Plasma-Based Accelerator Concepts," *IEEE Transactions on Plasma Science,* ***24*** *(2)*, 1996.

[28] R. Keinigs, Michael E. Jones, "Two-dimensional dynamics of the plasma wakefield accelerator," *Physics of Fluids,* ***30*** *(1)*, 1987.

[29] W. Lu et al., "Limits of linear plasma wakefield theory for electron or positron beams," *Physics of Plasmas,* ***12*** *063101*, 2005.

[30] V. S. Popov, "Tunnel and multiphoton ionization of atoms and ions in a strong lase field (Keldysh theory)," *Physics-Uspekhi,* ***47*** *(9) 855-855*, 2004.

[31] J. T. Moody et al., "Multi Keldysh regime resonant ionizing laser pulse propagation through a ten meter Rubidium vapor source at AWAKE," *talk presented at COFIL, Geneva, Switzerland*, 2018.

[32] M. Turner et al., "Experimental observation of plasma wakefield growth driven by the seeded self-modulation of a proton bunch," arXiv:1809.01191, accepted: *Physical Review Letters.*

[33] M. Turner, Ph.D. Thesis, Graz University of Technology.

[34] K. Rieger et al., "Experimental observation of proton bunch modulation in a plasma, at varying plasma densities," arXiv:1809.04478, accepted in: *Physical Review Letters.*

[35] C. Patrignani et al. (Particle Data Group), "Passage of particles through matter," *Chinese Physics C,* ***40****, 100001*, 2016.

[36] Lecture's notes, Particle Detectors course, University of Milan.

[37] E.A. Uehling, "Penetration of Heavy Charged Particles in Matter," *Annual Review of Nuclear and Particle Science,* ***4*** *315*, 1954.

[38] W. R. Leo, *Techniques for Nuclear and Particle Physics Experiment*, ch. Scintillation Detectors. Springer-Verlag Berlin Heidelberg, 1994.

[39] A. Ferrari et al., "FLUKA: A Multi-Particle Transport Code," *CERN-2005019, INFN/*$TC_0 5/11, SLAC - R - 773$.

[40] Beam Instrumentation Group , *CERN, private communication.*

[41] ELJEN TECHNOLOGY , *EJ-200 Datasheet.*

[42] J. S. Schmidt et al., “The AWAKE electron primary beam line,” *Proceedings of IPAC*, 2015.

[43] K. Pepitone et al., “The electron accelerators for the AWAKE experiment at CERN-Baseline and Future Developments,” *Nuclear Instruments and Methods in Physics Research A,* ***909*** *102-106*, 2018.

[44] E.A. Uehling, “Review of Emittance Diagnostics for Space Charge Dominated Beams for AWAKE e- Injector,” *Proceedings of IPAC*, 2016.

[45] C. Bracco, F. Velotti , *CERN, private communication.*

[46] P. Muggli et al., “Collective refraction of a beam of electrons at a plasma-gas interface,” *Physical Review Special Topics - Accelerators and Beams,* ***4*** *091301*, 2001.

[47] T. Bohl , *CERN, private communication.*

Thanks & Acknowledgments

To everybody who contributed to this work goes my most profound gratitude.
Particularly, I would like to thank my CERN supervisor Marlene Turner for supporting and encouraging me, with extreme patience and professionalism, always keeping in mind the difficulties of a student entering the research world for the first time. Without her, her passion and her dedication, this thesis would have never been possible.
Thanks to Edda Gschwendtner, AWAKE project leader, for offering me the outstanding opportunity of working at CERN during this year, and the coming ones.
Thanks to my advisor Professor Sorbi for supervising this thesis.
Thanks to the CERN Beam Instrumentation group for kindly providing the detectors I used in this work.
Thanks to Alexey, Barney, Fabian, Falk, Fearghus, Josh, Mathias, Misha, Patric, Spencer, and the whole AWAKE experimental team for welcoming me as a family and for making this work a path of personal growth, not only professional.
A special thanks to Anna-Maria, Felipe and James for being not only my *kindergarten* mates, but also the friends I needed when I didn't expect it.
Thanks to Nicolò and Simone for being, always, my *brothers in arms.*
Thanks to Lucia for always being there, linking dots with me.
Finally, I thank my parents, my sister and her husband for always supporting me, with unconditional love, on all my initiatives. I owe you everything.

Ringraziamenti

A tutti coloro che hanno contribuito a questo lavoro va la mia più profonda gratitudine.

In particolare, desidero ringraziare la mia relatrice esterna Marlene Turner per avermi seguito ed incoraggiato, con estrema pazienza e professionalità, tenendo sempre a mente le difficoltà di uno studente che si affaccia per la prima volta sul mondo della ricerca. Senza lei, la sua passione e la sua dedizione, questa tesi non sarebbe mai stata possibile.

Grazie a Edda Gschwendtner, AWAKE project leader, per avermi offerto la straordinaria possibilità di lavorare al CERN durante questo anno, e quelli a venire.

Grazie al mio relatore Professor Sorbi per aver sostenuto questa tesi.

Grazie al CERN *Beam Instrumentation group* per aver gentilmente messo a disposizione i rivelatori che ho utilizzato in questo lavoro.

Grazie a Alexey, Barney, Fabian, Falk, Fearghus, Josh, Mathias, Misha, Patric, Spencer, e tutto l'*experimental team* di AWAKE per avermi accolto come una famiglia e per aver reso questo lavoro un percorso di crescita personale, oltre che professionale.

Un grazie speciale ad Anna-Maria, Felipe e James per essere stati non solo i miei compagni di *kindergarten*, ma anche gli amici di cui avevo bisogno, quando non lo aspettavo.

Grazie a Nicolò e Simone per essere, sempre, i miei *brothers in arms.*

Grazie a Lucia per essere sempre stata lí, ad unire i puntini con me.

Infine, ringrazio i miei genitori, mia sorella e suo marito per avermi sempre sostenuto, con amore incondizionato, in ogni mio slancio e iniziativa. A voi devo tutto.